



AFRL-RQ-WP-TP-2015-0095

**INVESTIGATION OF LOW-PRESSURE TURBINE
ENDWALL FLOWS: SIMULATIONS AND EXPERIMENTS
(POSTPRINT)**

R. Sondergaard

**Turbomachinery Branch
Turbine Engine Division**

A. Gross

New Mexico State University

JANUARY 2015

Approved for public release; distribution unlimited.

See additional restrictions described on inside pages

STINFO COPY

**AIR FORCE RESEARCH LABORATORY
AEROSPACE SYSTEMS DIRECTORATE
WRIGHT-PATTERSON AIR FORCE BASE, OH 45433-7541
AIR FORCE MATERIEL COMMAND
UNITED STATES AIR FORCE**

NOTICE AND SIGNATURE PAGE

Using Government drawings, specifications, or other data included in this document for any purpose other than Government procurement does not in any way obligate the U.S. Government. The fact that the Government formulated or supplied the drawings, specifications, or other data does not license the holder or any other person or corporation; or convey any rights or permission to manufacture, use, or sell any patented invention that may relate to them.

This report was cleared for public release by the USAF 88th Air Base Wing (88 ABW) Public Affairs Office (PAO) and is available to the general public, including foreign nationals.

Copies may be obtained from the Defense Technical Information Center (DTIC)
(<http://www.dtic.mil>).

AFRL-RQ-WP-TP-2015-0095 HAS BEEN REVIEWED AND IS APPROVED FOR
PUBLICATION IN ACCORDANCE WITH ASSIGNED DISTRIBUTION STATEMENT.

*//Signature//

ROLF SONDERGAARD
Project Manager
Electrical Systems Branch
Power and Control Division

//Signature//

ROLF SONDERGAARD, Acting Chief
Electrical Systems Branch
Power and Control Division
Aerospace Systems Directorate

//Signature//

CHARLES W. STEVENS
Lead Engineer
Power and Control Division
Aerospace Systems Directorate

This report is published in the interest of scientific and technical information exchange, and its publication does not constitute the Government's approval or disapproval of its ideas or findings.

*Disseminated copies will show “//Signature//” stamped or typed above the signature blocks.

REPORT DOCUMENTATION PAGE				Form Approved OMB No. 0704-0188	
<p>The public reporting burden for this collection of information is estimated to average 1 hour per response, including the time for reviewing instructions, searching existing data sources, gathering and maintaining the data needed, and completing and reviewing the collection of information. Send comments regarding this burden estimate or any other aspect of this collection of information, including suggestions for reducing this burden, to Department of Defense, Washington Headquarters Services, Directorate for Information Operations and Reports (0704-0188), 1215 Jefferson Davis Highway, Suite 1204, Arlington, VA 22202-4302. Respondents should be aware that notwithstanding any other provision of law, no person shall be subject to any penalty for failing to comply with a collection of information if it does not display a currently valid OMB control number. PLEASE DO NOT RETURN YOUR FORM TO THE ABOVE ADDRESS.</p>					
1. REPORT DATE (DD-MM-YY) January 2015		2. REPORT TYPE Conference Proceedings Postprint		3. DATES COVERED (From - To) 01 January 2015 – 01 January 2015	
4. TITLE AND SUBTITLE INVESTIGATION OF LOW-PRESSURE TURBINE ENDWALL FLOWS: SIMULATIONS AND EXPERIMENTS (POSTPRINT)				5a. CONTRACT NUMBER In-house	
				5b. GRANT NUMBER	
				5c. PROGRAM ELEMENT NUMBER 61102F	
6. AUTHOR(S) R. Sondergaard (AFRL/RQTT) A. Gross (New Mexico State University)				5d. PROJECT NUMBER 3002	
				5e. TASK NUMBER N/A	
				5f. WORK UNIT NUMBER Q1BS	
7. PERFORMING ORGANIZATION NAME(S) AND ADDRESS(ES) Turbomachinery Branch (AFRL/RQTT) Turbine Engine Division Air Force Research Laboratory, Aerospace Systems Directorate Wright-Patterson Air Force Base, OH 45433-7541 Air Force Materiel Command, United States Air Force			New Mexico State University Las Cruces, NM 88011 8. PERFORMING ORGANIZATION REPORT NUMBER AFRL-RQ-WP-TP-2015-0095		
9. SPONSORING/MONITORING AGENCY NAME(S) AND ADDRESS(ES) Air Force Research Laboratory Aerospace Systems Directorate Wright-Patterson Air Force Base, OH 45433-7541 Air Force Materiel Command United States Air Force				10. SPONSORING/MONITORING AGENCY ACRONYM(S) AFRL/RQTT	
				11. SPONSORING/MONITORING AGENCY REPORT NUMBER(S) AFRL-RQ-WP-TP-2015-0095	
12. DISTRIBUTION/AVAILABILITY STATEMENT Approved for public release; distribution unlimited.					
13. SUPPLEMENTARY NOTES PA Case Number: 88ABW-2014-5565; Clearance Date: 01 Dec 2014. This conference paper was published in the proceedings of the 53rd AIAA Aerospace Sciences Meeting (AIAA) Conference, held January 5 - 9, 2015 in Kissimmee, FL. The U.S. Government is joint author of the work and has the right to use, modify, reproduce, release, perform, display, or disclose the work.					
14. ABSTRACT Highly loaded low-pressure turbine (LPT) blades offer opportunities for lower costs and higher performance but suffer from unacceptable endwall losses. This has motivated research aimed at reducing the endwall losses by manipulating the passage vortex that constitutes the primary source of losses. Passive approaches, such as prole and endwall contouring or active flow control, did reduce endwall losses but require a more detailed understanding of the underlying flow physics to be better optimized. Endwall research also suffers from a lack of temporal and spatial resolution of the existing flow data which limits the depth of the physical analysis. LPT endwall flow experiments at the Air Force Research Laboratory revealed the mean flow features but did not resolve the unsteady flow structures. Therefore, the decision was made to carry out endwall simulations with a higher-order-accurate Navier-Stokes code and to investigate the underlying hydrodynamic instabilities. In this paper, results from endwall flow simulation for the L2F geometry with and without endwall fillet are presented. Both a turbulent and a laminar endwall boundary layer are being considered. For the former, a passage vortex is generated at the endwall. The addition of the fillet suppresses the vortex. For the laminar endwall boundary layer, without fillet the passage vortex is missing. This interesting result indicates a strong dependence of the flow topology on the endwall boundary layer properties.					
15. SUBJECT TERMS endwall, low-pressure turbine, blade					
16. SECURITY CLASSIFICATION OF:			17. LIMITATION OF ABSTRACT:	18. NUMBER OF PAGES	19a. NAME OF RESPONSIBLE PERSON (Monitor) Rolf Sondergaard 19b. TELEPHONE NUMBER (Include Area Code) N/A
a. REPORT Unclassified	b. ABSTRACT Unclassified	c. THIS PAGE Unclassified			

Investigation of Low-Pressure Turbine Endwall Flows: Simulations and Experiments

A. Gross*

New Mexico State University, Las Cruces, NM 88011

R. Sondergaard†

U.S. Air Force Research Laboratory, Wright-Patterson Air Force Base, OH 45433

Highly loaded Low-Pressure Turbine (LPT) blades offer opportunities for lower costs and higher performance but suffer from unacceptable endwall losses. This has motivated research aimed at reducing the endwall losses by manipulating the passage vortex which constitutes the primary source of losses. Passive approaches such as profile and endwall contouring or active flow control did reduce endwall losses but require a more detailed understanding of the underlying flow physics to be better optimized. Endwall research also suffers from a lack of temporal and spatial resolution of the existing flow data which limits the depth of the physical analysis. LPT endwall flow experiments at the Air Force Research Laboratory revealed the mean flow features but did not resolve the unsteady flow structures. Therefore the decision was made to carry out endwall simulations with a higher-order-accurate Navier-Stokes code and to investigate the underlying hydrodynamic instabilities. In this paper results from endwall flow simulation for the L2F geometry with and without endwall fillet are presented. Both a turbulent and a laminar endwall boundary layer are being considered. For the former a passage vortex is generated at the endwall. The addition of the fillet suppresses the vortex. For the laminar endwall boundary layer, without fillet the passage vortex is missing. This interesting result indicates a strong dependence of the flow topology on the endwall boundary layer properties.

I. Introduction

The Low-Pressure Turbine (LPT) produces the bulk net power in many jet engines.¹ The LPT-driven fan is responsible for up to 80% of the total engine thrust and the LPT can constitute as much as one third of the overall engine weight.² Changes in LPT efficiency can result in nearly equal changes in overall engine efficiency. Modern LPTs have to drive larger fans at lower fan speeds and, at the same time, have to be less complex and lighter. The goal in modern jet engine development is a reduction in LPT stage solidity without compromising performance. The LPT blade count is limited by the blade loading. A higher loading would allow for a reduction of the overall engine cost and weight and/or a performance increase. Ultimately, the economics of air travel would be improved. Towards this end highly loaded LPT blades are being developed, with loading approaching twice the currently fielded levels.

LPTs must operate efficiently over a large range of Reynolds numbers. Low Reynolds number operating conditions in combination with aggressive designs can lead to laminar separation from the suction side, which can cause significant reductions in turbine and overall engine performance. Highly loaded blades are typically front-loaded to counteract laminar separation from the suction side. Front-loading results in a less aggressive suction side pressure recovery and thus increases stall resistance at low Reynolds numbers. Front-loading can be achieved by increasing the stagger angle (chord angle relative to the incoming flow) or, for a fixed stagger angle, by thickening the leading edge (e.g., Korakianitis³ and Korakianitis and Papagiannidis⁴). An example of a highly loaded design is the L2F profile which was developed at the Air Force Research Laboratory (AFRL) at Wright-Patterson Air Force Base.

*Assistant Professor. Mechanical and Aerospace Engineering. Senior Member AIAA.

†Aerospace Engineer. Lead Scientist. Propulsion Directorate. Senior Member AIAA.

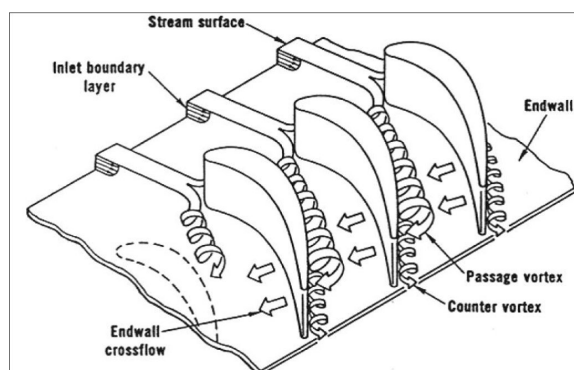


Figure 1. Sketch of endwall flow from Langston.⁷

Unfortunately, for the aspect ratios encountered in typical gas turbine engines, front-loaded airfoils with high stagger angle suffer from unacceptable endwall losses (i.e., secondary flow losses). For that reason, highly loaded profiles which promise to reduce the engine parts count have never been employed in production engines. The endwall flow is highly complex (e.g., Sieverding,⁵ Wang et al.,⁶ Langston⁷) and characterized by the passage vortex which is the dominant feature, the horseshoe vortex, the counter vortex, and the endwall crossflow among others (Fig. 1).

Increased endwall losses for front-loaded profiles were observed by a large number of researchers, e.g., Weiss and Fottner,⁸ Zoric et al.,⁹ and Knezivici et al.¹⁰ For example, Praisner et al.¹¹ found high endwall losses for the Pack DF high lift design which has a 25% higher loading than the (conventional) Pack B blade. The front-loaded profiles in these earlier investigations were designed with increased stagger angles compared to the companion aft-loaded profiles. Results by Lyall¹² indicate that the high stagger angle and not the front-loading is responsible for the endwall losses. High stagger profiles tend to produce a larger “blockage” for the incoming endwall boundary layer flow (stronger adverse pressure gradient) thereby aggravating endwall separation and resulting in more fluid being entrained in the endwall vortices.

Endwall losses are common to all gas turbines stages and several passive flow control techniques have been proposed to alleviate them (for a review see Langston⁷), among them boundary layer fences, leading edge bulbs and fillets (e.g., Sauer et al.,¹³ Zess and Thole,¹⁴ Becz et al.,¹⁵ Saha et al.,¹⁶), skewing or compound leaning of the airfoil (e.g., Harrison¹⁷), and endwall contouring (e.g., Rose,¹⁸ Harvey et al.,¹⁹ Hartland et al.,²⁰ Praisner²¹). These methods aim to reduce the endwall losses by manipulating the endwall vortex structures to reduce the total pressure loss.

Endwall contouring (or profiling) where non-axisymmetric endwalls are used in an attempt to modify the flow has been investigated extensively for high-pressure turbines (e.g., the “Durham cascade,” Bagshaw et al.²²). For example, Harvey et al.¹⁹ employed non-axisymmetric endwall contouring to decrease the cross-passage pressure gradient which weakened the passage vortex and reduced the total pressure loss. McIntosh et al.²³ employed a genetic algorithm for optimizing the endwall shape. The technology has progressed considerably and is beginning to see implementation on the most recent engines (e.g., Trent 900). Endwall contouring does, however, not seem to work sufficiently for highly loaded LPT profiles. For example, Knezevici et al.¹⁰ and Praisner et al.¹¹ found that endwall losses remained beyond practical limits for the high lift Pack DF profile, even after implementing non-axisymmetric endwall contouring. Other approaches such as profile contouring (or combinations of different approaches) have to be considered to reduce the endwall losses of high lift LPT designs to acceptable levels. As described by Langston,⁷ the concept of leading edge bulbs is to strengthen the counter vortex, which has the opposite sense of rotation of the passage vortex, thus weakening the overall vortex system that comprises the endwall flow. On the other hand, Zess and Thole¹⁴ showed that a leading edge fillet can reduce or eliminate the horseshoe vortex that forms as the inlet boundary layer separates. Becz et al.¹⁵ accomplished nearly the same aerodynamic loss reduction with both a leading edge bulb and a fillet.

The AFRL decided to investigate profile contouring to reduce the endwall losses (e.g., Lyall et al.²⁴ and Sangston et al.²⁵). A new geometry was designed that blends from a L2F profile inside the passage to a low-stagger L2F-LS airfoil near the endwall. The “combined” geometry was designated L2F-EF. This design choice was made based on the observation that a reduction of the stagger angle near the endwall would

weaken the endwall vortices and lower the endwall losses. Contouring the L2F airfoil at the endwall to obtain the benefit of low stagger angle generates a fillet that extends out from the pressure surface, primarily in the pitchwise direction toward the adjacent suction surface. Experiments for $Re=100,000$ showed an approximate 10% reduction of the total pressure loss coefficient for the contoured L2F-EF airfoil.¹² Since AFRL is carrying out detailed flow field measurements for this configuration it was chosen for the present simulations.

The profile contouring in the AFRL design did reduce endwall losses but requires a more detailed understanding of the endwall flow physics to be better optimized. Reynolds-Averaged Navier-Stokes (RANS) calculations that were carried out during the design process²⁴ provided reasonably accurate mean flow predictions but suffered from the following shortcomings: By design most RANS models cannot capture transition which has been found to play a dominant role in LPT flows. By assuming fully turbulent flow, the laminar separation bubble that can naturally occur on the suction surface is suppressed. Laminar separation bubbles not only transition the flow. They also act as natural “oscillators” and shed coherent structures which introduce a large amount of unsteadiness into the flow. In RANS calculations this unsteadiness is inhibited because the bubble is not captured. In addition, since RANS models are derived under the assumption that all unsteady motion is modeled, they typically introduce a large amount of turbulent eddy viscosity which dampens out all or most of the unsteadiness. As a result not all of the relevant flow physics are captured in RANS calculations. Simulations of high-lift LPT endwall flows at low Reynolds numbers are quite challenging primarily due to the intricate interaction of transition and separation. Direct Numerical Simulations (DNS; the highest fidelity approach) or Implicit Large Eddy Simulations (ILES) that capture the essential flow physics at reduced computational cost appear to be the most feasible alternatives. As far as LPT simulations with endwall are concerned, P. Tucker and co-workers at Cambridge University (UK) in collaboration with Rolls-Royce appear to be the only ones that have carried out a time-accurate simulation of a LPT cascade with endwall. Some flow visualizations are available online but to the authors best knowledge none of the results have been published.

In this paper results from time-resolved high-resolution endwall flow simulation for the L2F and L2F-EF geometries are presented. First the methods employed for generating the computational grid and the turbulent endwall boundary layer are explained. Then simulation results for a turbulent and a laminar endwall boundary layer are presented and the total pressure loss coefficients for the various cases are compared. The paper concludes with a brief summary and conclusions.

II. Methodology

A. Simulated Cases

Simulations were carried out for the L2F blade which was developed at AFRL for investigating the low-Reynolds number and high lift LPT aerodynamics.²⁶ The design intent was to have good low-Reynolds number performance compared to the Pratt and Whitney Pack B blade and high aerodynamic lift. The axial blade chord and span in the AFRL experiments²⁵ were $C_x=6\text{in}$ and $H=3.5C_x$ (21in), respectively. The pitchwise spacing was $1.221C_x$ and thus 38% larger than for the Pack B blade. The L2F blade has a design inflow angle of 35deg and an exit angle of -58.12deg. The stagger angle is 34.60deg. In addition, the L2F-EF geometry (L2F with endwall fillet) was considered which blends from a L2F airfoil at mid-span to a L2F-LS at the endwall.²⁴ The blending extends over 9.5% of the total span ($=0.3325C_x$) at both endwalls. The simulations were set up according to the AFRL experiments where upstream wakes and surface roughness were not considered. This deliberate simplification, when compared to the environment in real jet engines, allows for an easier extraction of the flow physics and a comparison with the experimental data. Only half of the blade span was simulated and symmetry conditions were enforced at mid-span. The Reynolds number based on axial chord, C_x , for the simulations was $Re=100,000$ and thus the same as in the experiments and earlier RANS calculations.^{24, 25}

B. Endwall Boundary Layer State

The endwall in the experiment had an elliptic leading edge with (in the axial direction) major semiaxis of $0.25C_x$ (1.5in) and (in the wall-normal direction) minor semiaxis of $0.0417C_x$ (0.25in). Measured in the axial direction, the flat plate leading edge was located at $x=-3.958C_x$ (23.75in) where the minus sign indicates a location upstream of the inflow plane of the cascade ($x=0$). The corresponding streamwise distance is $s=-3.958/\cos 35\text{deg}=-4.833C_x$ (29in). The displacement thickness, $\delta^* = \int (1 - v/v_\infty) dy$, for a laminar flat

plate boundary layer is $\delta^* = 1.721s/Re_s^{0.5}$. For $s = 4.833C_x$, $Re_{\delta^*} = 1.721\sqrt{s/C_x Re} = 1,200$. At this Reynolds number (for the experimental freestream turbulence intensity, FSTI=1%) the boundary layer (at the cascade inlet plane) can be expected to be turbulent.

In the RANS calculations by Lyall et al.²⁴ a turbulent boundary layer with a thickness of $\delta_{99}=0.025H=0.0875C_x$ was prescribed at the inflow boundary which was located at $x=-1.4C_x$. The following approximations hold for a turbulent flat plate boundary layer:

$$\delta_{99} = \frac{0.37s}{Re_s^{0.2}}, \quad \delta^* = \frac{0.046s}{Re_s^{0.2}}, \quad \theta = \frac{0.036s}{Re_s^{0.2}}, \quad \text{and} \quad c_f = \frac{0.0592}{Re_s^{0.2}}. \quad (1)$$

Accordingly, the distance to the “virtual leading edge” (measured in the streamwise direction) for the Lyall et al. calculations is $s/C_x=(1/0.37 \delta_{99}/C_x Re^{0.2})^{1/0.8}=2.933$. Relative to the inflow plane of the cascade, the virtual leading edge is located at $x=-2.933 \times \cos 35\text{deg}-1.4=-3.802C_x$. From the inflow velocity profiles of the Lyall et al. calculations²⁴ the displacement and momentum thickness were computed as $\delta^*=0.012543C_x$ and $\theta=0.0092353C_x$ which corresponds to $s/C_x=3.504$ ($x=-4.270C_x$) and $s/C_x=3.247C_x$ ($x=-4.060C_x$).

The endwall in the experiments is segmented (i.e., modular) and different upstream lengths are possible. The shortest possible upstream extent of the endwall is $0.683C_x$ (4.1in) in the axial direction and $0.834C_x$ (5in) in the streamwise direction. The corresponding Reynolds number based on displacement thickness is $Re_{\delta^*}=497$. At this Reynolds number the boundary layer (at the cascade inlet plane) is likely laminar.

C. Navier-Stokes Code

A research computational fluid dynamics code that was developed in our laboratory was employed for the present investigations.²⁷ The code solves the compressible Navier-Stokes equations in the finite volume formulation. The convective terms were discretized with a ninth-order-accurate upwind scheme (unless stated otherwise). The viscous terms were discretized with a fourth-order-accurate scheme. A second-order-accurate implicit Adams-Moulton method was employed for time integration.

D. Normalization

Length scales were made dimensionless with the axial chord length, C_x . Velocities were made dimensionless with the cascade inflow velocity, v_∞ . Density was made dimensionless with the inflow density, ρ_∞ , and pressure was made dimensionless with $\rho_\infty v_\infty^2$. Time was made dimensionless with C_x/v_∞ . The reference Mach number was $M=0.1$. This Mach number is small enough to satisfy the incompressible flow assumption without negatively affecting the convergence characteristics of the implicit time-integration scheme. The Prandtl number was $Pr=0.72$.

E. Computational Grids

Two different computational grids were generated with a Poisson grid generator²⁸ (Fig. 2). The block boundaries are outlined in red. Both grids are periodic in the pitchwise direction. The virtual flat plate leading edge is indicated by a bold vertical line. The first grid (grid 1) consists of four blocks and extends upstream to $x=-2.9536$. This grid was created for the case where the endwall leading edge is at $x=-3.958$ and the endwall boundary layer is turbulent. The second grid (grid 2) consists of two blocks and extends upstream to $x=-0.5$. This grid was designed for the case where the endwall leading edge is at $x=-0.6833$ and the endwall boundary layer is laminar. For both grids, streamwise grid line stretching was employed near the outflow to dissipate wake structures. Also for both grids, singular points are obtained where the central O-grids connect with each other. The block grid resolutions are provided in Tab. 1. For block 1 the number of cells in the wall-normal direction is larger for grid 1 compared to grid 2. This was mainly done to obtain a reasonable pitchwise grid resolution for block 4 with a cell aspect ratio (streamwise to pitchwise) close to one.

For the 3-D simulations (without endwall fillet) the 2-D grids were “extruded” in the spanwise direction. For both cases $K=256$ cells were employed in the spanwise direction. The total number of cells was 15.2 million for the turbulent case (grid 1) and 9.27 million for the laminar case (grid 2). For comparison, 713 thousand cells were employed for the calculations by Lyall et al.²⁴ The wall-normal grid line spacing at the endwall was $\Delta z = 10^{-4}C_x$. A grid line distribution that provides grid line clustering near the endwall

$$z_0 = 0 \quad (2)$$

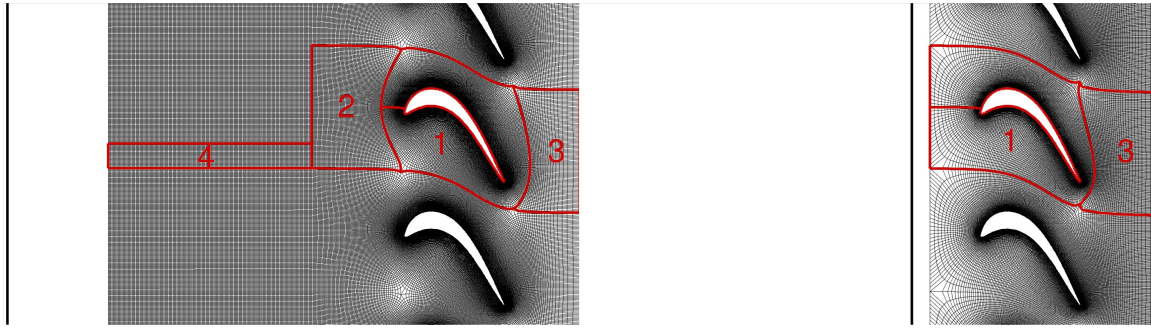


Figure 2. Details of computational grid for turbulent case (left, grid 1) and laminar case (right, grid 2).

Block	Turbulent case, grid 1	Laminar case, grid 2
1	400×120	400×80
2	60×100	
3	20×100	30×140
4	160×20	
total	59,200	36,200

Table 1. Number of cells per block.

$$z_1 = \Delta z \quad (3)$$

$$z_k = z_{k-1} + \left[0.1 \left(\frac{k-K}{2-K} \right)^c + 1 \right] (z_{k-1} - z_{k-2}) \quad \text{for } k \geq 2 \quad (4)$$

and blends towards an equidistant spacing near mid-span was employed in the spanwise direction. The near-

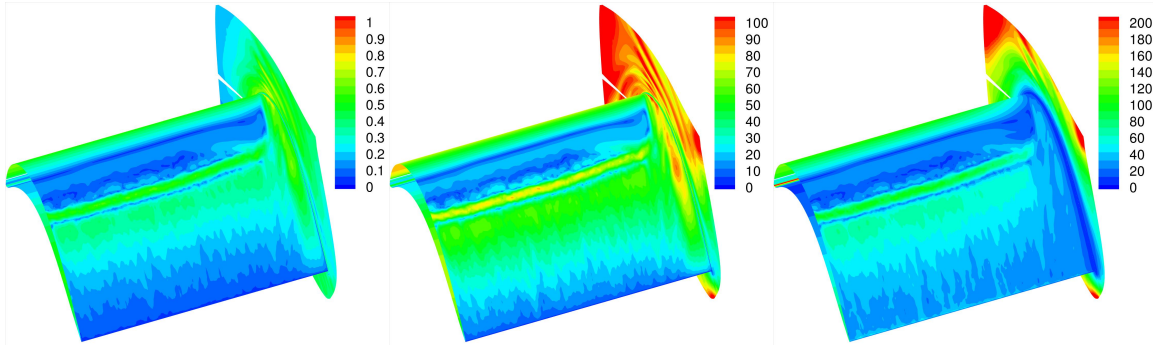


Figure 3. Near-wall grid resolution in wall units (From left to right: Wall-normal/ circumferential/ spanwise-radial).

wall grid resolution for the coarser grid (grid 2) is provided in Fig. 3. The wall-normal near-wall grid line spacing is less than one. The circumferential (streamwise) grid line spacing in wall units at the wall is less than 80 and the spanwise grid line spacing is about 100. Georgiadis et al.²⁹ recommend a grid resolution of $50 \leq \Delta x^+ \leq 150$, $\Delta y^+ \leq 1$, $15 \leq \Delta z^+ \leq 40$ for Large Eddy Simulations (LES). Accordingly the streamwise and wall-normal resolution of the present grid is sufficient. To meet the Δz^+ requirement, the spanwise grid resolution would have to be increased 2.5 times. The near-wall resolution for the grid 1 (turbulent case) is slightly higher and not shown.

For the L2F-EF geometry the LPT coordinates of the computational grid by Lyall et al.²⁴ were splined in the z -direction and $z=\text{const.}$ slices were extracted (Fig. 4). For each slice a 2-D grid was generated with the Poisson grid generator. In between the z -slices shown in Fig. 4 the grid points were interpolated (in the spanwise direction) using either Hermite or Bezier splines. The Bezier splines did (by design) not exactly

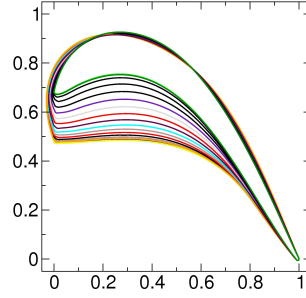


Figure 4. Slices of constant z for L2F-EF geometry.

pass through the control points but resulted in an overall higher grid quality (Fig. 5). Considering the relatively low geometry information content of the source grid (limited number of z -planes) the fact that the Bezier-spline-based grid missed the control points by a very small amount (this was confirmed visually) was determined acceptable. In the following, the grid with fillet derived from grid 1 (turbulent endwall boundary layer) is referred to as grid 3 and the grid derived from grid 2 (laminar endwall boundary layer) is referred to as a grid 4. The number of cells per block remains unchanged.

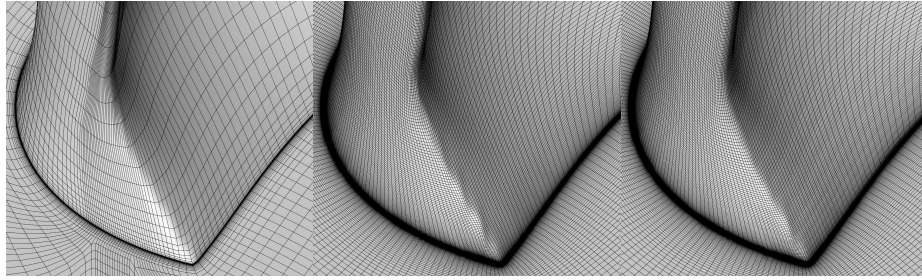


Figure 5. From left to right: 1) Lyall et al.²⁴ grid; 2) Hermite spline grid; 3) Bezier spline grid.

F. Boundary Conditions

Walls were considered as adiabatic. Non-reflecting boundary conditions³⁰ were applied at the inflow and outflow boundary. Symmetry was enforced at mid-span (only half of the passage span was simulated). Periodicity conditions were applied in the pitchwise direction.

1. Turbulent Endwall Boundary Layer

The purpose of block 4 for grid 1 (Fig. 2) was to obtain an equilibrium turbulent boundary layer at the inflow to block 3. A Blasius velocity profile with $Re_s = 264,810$ was prescribed at the inflow boundary of block 4. A forcing slot of length L_x was added near the inflow boundary of block 4 to introduce disturbances into the boundary layer (the forcing slot is highlighted in black in Fig. 6). Wall-normal blowing and suction with

$$w_{forcing} = a_x \sum_i A_i \cos(\alpha_i x + \beta_i y - \omega_i t) \quad (5)$$

and axial and pitchwise wavenumbers of $\alpha_i = 2\pi/\lambda_{i,x}$ and $\beta_i = 2\pi/\lambda_{i,y}$ was applied for $-2.8901 < x < -2.7631$. A half-sine shaped amplitude distribution was prescribed in the axial direction, $a_x = \sin((x + 2.8901)/L_x \pi)$. It was decided to force a Tollmien-Schlichting wave and a steady 3-D disturbance. Diagrams found in Baines et al.³¹ provided guidance for the selection of the period and wavelength of the traveling wave. Several parameter combinations were tried. The combination in Tab. 2 resulted in a rapid breakdown of the endwall

i	λ	λ_x	λ_y	ω	A
1	0.2	$\frac{\lambda}{\cos 35deg}$	$\frac{\lambda}{\sin 35deg}$	$\frac{2\pi}{0.1}$	0.1
2	$0.1221 \times \cos 35deg$	$\frac{-\lambda}{\sin 35deg}$	$\frac{\lambda}{\cos 35deg}$	0	0.1

Table 2. Forcing parameters.

boundary layer. A visual representation of the endwall boundary layer is provided in Fig. 6. For the ninth-order-accurate discretization a larger wavenumber interval is resolved (compared to the fifth-order-accurate discretization). Time- and pitchwise-averaged velocity profiles near the outflow boundary of block 4 are

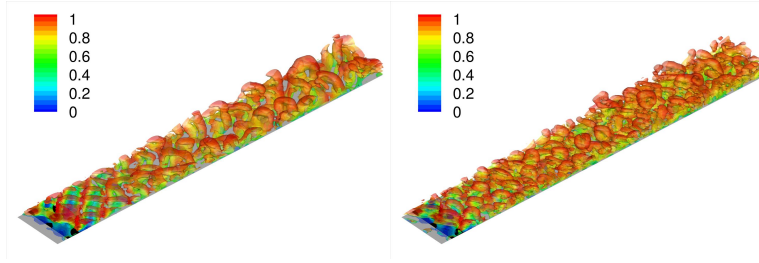


Figure 6. Block 4 endwall boundary layer. Iso-surfaces of $Q=1$ colored by velocity magnitude obtained with fifth- and ninth-order-accurate scheme (left and right).

shown in Fig. 7. As a reference, the relationships for the viscous sublayer, $u^+ = y^+$, and for the log-layer,

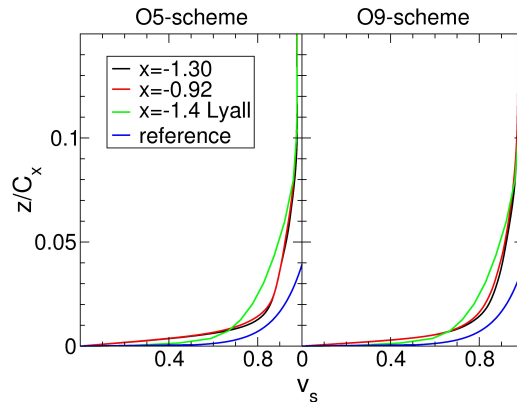


Figure 7. Block 4 velocity profiles.

$u^+ = 5 + 1/0.41 \ln y^+$ were included. For $x=-1.4$, $Re_s=312,000$ and $c_f=0.00471$ are obtained and the profiles are scaled according to $u/u_\infty = \sqrt{c_f/2} \times u^+$ and $z/C_x = \sqrt{2/c_f/Re} \times z^+$. In the present ILES only the larger flow structures are resolved and numerical diffusion dampens out much of the high wavenumber spectral content. As a result the near-wall Reynolds-stresses are underpredicted. The skin-friction coefficient is shown in Fig. 8. Also included are reference lines for a laminar ($c_f = (C_x/s)^{0.5} 0.664/Re^{0.5}$) and a turbulent boundary layer ($c_f = (C_x/s)^{0.2} 0.0592/Re^{0.2}$) starting from the endwall leading edge. Downstream of the forcing slot the skin-friction coefficient displays a mild oscillation which can be attributed to the forced steady 3-D mode which is decaying in the streamwise direction. Overall the skin friction coefficient is too low although the mismatch is less severe for the more accurate discretization.

The displacement and momentum thickness were computed for four downstream locations (Tab. 3). Also included in the table is the shape factor $H = \delta^*/\theta$. As a reference, from the Lyall et al.²⁴ data $\delta^*=0.012$, $\theta=0.0091$, and $H=1.36$ were extracted for $x=-1.4$. The relationships for the turbulent boundary layer (Eqs. 1) provide $\delta^*=0.011$, $\theta=0.0089$, and $H=1.27$. Compared to these reference data, both displacement and momentum thickness for the present simulations are too too small. The difference is less for the ninth-order

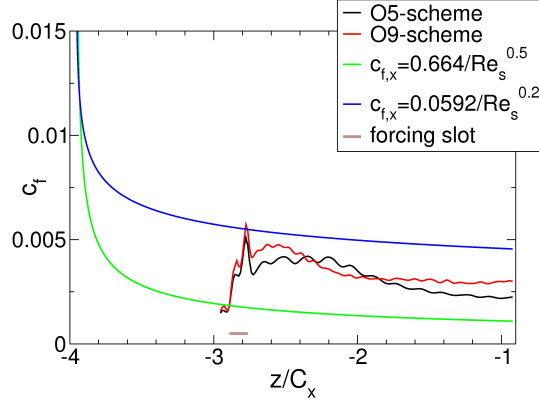


Figure 8. Block 4 skin-friction coefficient for $Re = 100,000$.

accurate scheme. The shape factor is smaller than 2.59 (Blasius boundary layer) but still larger than what would be expected for a turbulent boundary layer ($H \approx 1.3$). Although the turbulent boundary layer in the

x/C_x	δ^*/C_x	θ/C_x	H
fifth-order-accurate scheme			
-1.303	0.0104	0.00659	1.57
-0.922	0.0109	0.00687	1.58
ninth-order-accurate scheme			
-1.303	0.0103	0.00690	1.50
-0.922	0.0112	0.00764	1.47

Table 3. Block 4 boundary layer properties.

present simulations does not accurately match the reference data the approach appears justified because of the considerable compute time savings compared to a fully-resolved DNS.

2. Laminar Endwall Boundary Layer

The smallest possible upstream extent of the endwall from the cascade inflow in the experiment is $x=-0.683$. The inflow boundary for grid 2 is at $x=-0.5$. The difference is 0.183 (in the axial direction) or $s=0.183/\cos 35\text{deg}=0.223$ in the streamwise direction. Accordingly, a Blasius velocity profile with $Re_s=22,300$ was prescribed at the inflow boundary of block 1.

G. Total Pressure Loss Coefficient

With the chosen non-dimensionalization the reference (inlet) dynamic and total pressure are

$$q_{ref} = \frac{1}{2} \rho_{ref} (u_{ref}^2 + v_{ref}^2 + w_{ref}^2) = \frac{1}{2} \quad (6)$$

$$p_{0,ref} = p_{ref} + q_{ref} = \frac{1}{\gamma M^2} + \frac{1}{2}. \quad (7)$$

The inflow and outflow dynamic and total pressure are

$$q_{in,out} = \frac{1}{2} \rho_{in,out} (u_{in,out}^2 + v_{in,out}^2 + w_{in,out}^2) \quad (8)$$

$$p_{0,in,out} = p_{in,out} + q_{in,out} = \frac{\rho_{in,out} T_{in,out}}{\gamma M^2} + q_{in,out}. \quad (9)$$

Approved for public release; distribution unlimited.

The total pressure coefficient is defined as

$$c_{p,0} = \frac{p_0 - p_{0,ref}}{q_{ref}}. \quad (10)$$

The mass-averaged total pressure coefficient was approximated as

$$c''_{p,0} = \frac{\iint \rho |\vec{v}| c_{p,0} dy dz}{\iint \rho |\vec{v}| dy dz} \approx \frac{\sum_i \rho |\vec{v}| c_{p,0} V_i}{\sum_i \rho |\vec{v}| V_i}, \quad (11)$$

where the sums were taken over the cell volumes, V_i , directly adjacent to the inflow/outflow boundary. The same procedure was applied for mass-averaging the dynamic pressure. The total pressure loss coefficient was computed as²⁵

$$Y_{tot} = c''_{p,0,in} - c''_{p,0,out}. \quad (12)$$

H. Location of Slices for Comparison with Sangston et al.²⁵ Measurements

Sangston et al.²⁵ acquired Particle Image Velocimetry (PIV) data in an outflow plane at $x=1.5C_x$ and in four planes normal to the chord line (Fig. 9). The L2F stagger angle is $\lambda=34.60^\circ$. The origin of the

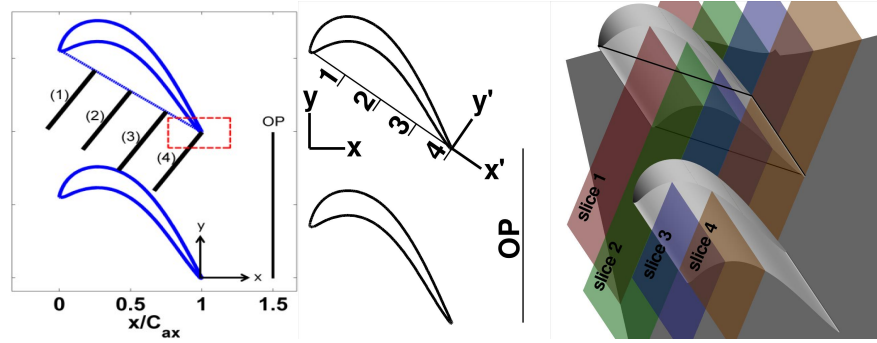


Figure 9. Slices where PIV data was obtained by Sangston et al.²⁵ Fig. 4a from Sangston et al.,²⁵ coordinate systems, and 3-D representation.

chord-normal slices is at $x_o=0.25, 0.5, 0.75, 1$ and $y_o = (1 - x_o) \tan \lambda$. The surface normal of the planes is $\vec{n} = [\cos \lambda, -\sin \lambda, 0]$. The coordinate transformation from (x, y, z) to (x', y', z') is

$$x' = (x - x_o) \cos \lambda - (y - y_o) \sin \lambda, \quad (13)$$

$$y' = (x - x_o) \sin \lambda + (y - y_o) \cos \lambda, \quad (14)$$

$$(15)$$

and $z'=z$. The vorticity in the x' direction is

$$\omega_{x'} = \omega_x \cos \lambda - \omega_y \sin \lambda. \quad (16)$$

III. Results

A. Turbulent Endwall Boundary Layer

1. Straight Blade (No Fillet)

Iso-surfaces of the Q vortex identification criterion at $t=6$ in Fig. 10 illustrate how the turbulent endwall boundary layer interacts with the blade. The vortex identification criterion,³²

$$Q = \frac{1}{2} (W_{ij}W_{ij} - S_{ij}S_{ij}), \quad (17)$$

indicates areas where rotation dominates strain. The endwall region near the suction side corner is relatively “quiet” while a large amount of flow structures is seen near the pressure side corner. The boundary layer on

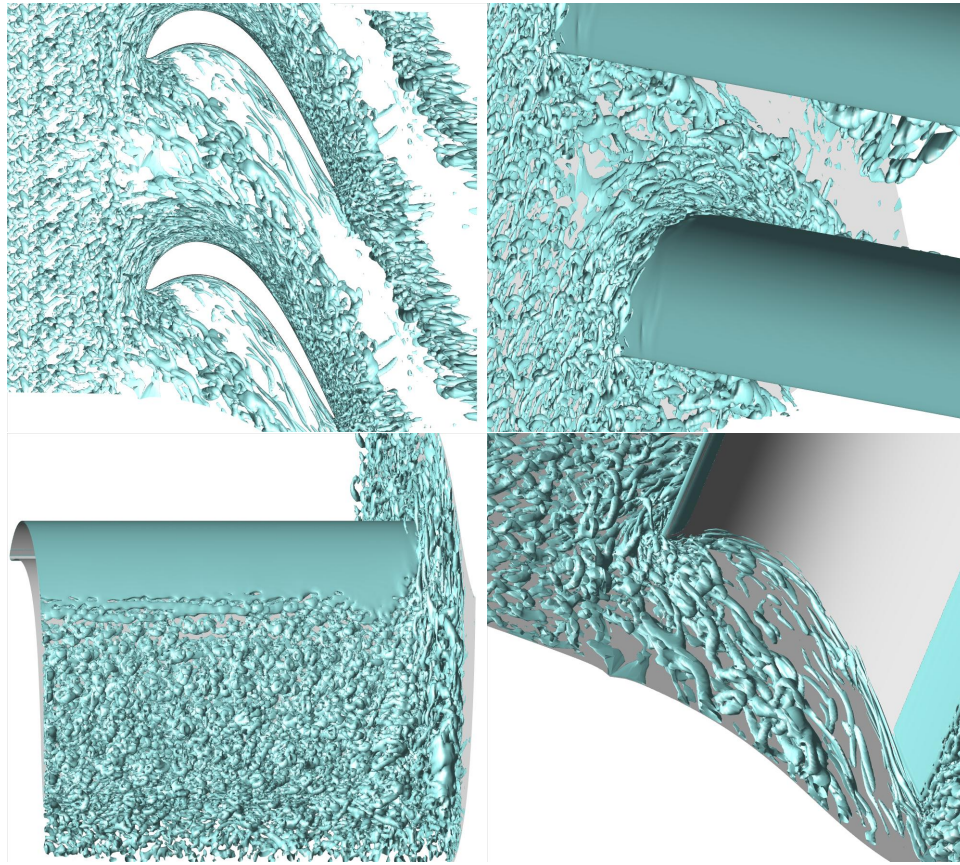


Figure 10. Instantaneous iso-surfaces of $Q = 10$.

the LPT blade (away from the wall) is laminar from the leading edge and remains laminar on the pressure side. The suction side boundary layer separates laminar approximately at the beginning of the “uncovered” turning. The separated boundary layer transitions rapidly and reattaches to the blade. Also noticeable is the pitchwise periodicity of the endwall structures at the inflow of block 2 that results from the relatively small pitchwise extent of block 4 (one fifth of the blade spacing).

In Fig. 11 skin-friction lines and streamlines computed from the time-average are overlaid with an instantaneous flow visualization. The skin-friction lines reveal a saddle point upstream of the leading edge which

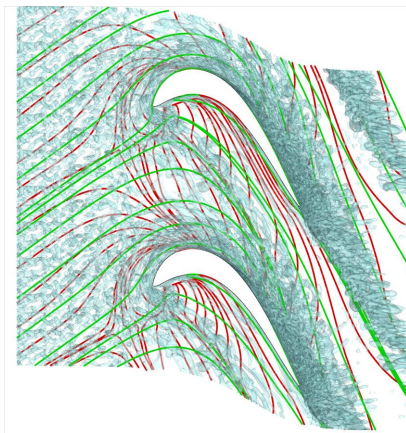


Figure 11. Instantaneous iso-surfaces of $Q = 10$, skin-friction lines (red lines), and streamlines (green lines).

indicates a three-dimensional (3-D) separation. In between the blades a line of separation is seen which must be associated with the passage vortex. The streamlines (computed from a $z = 0.05$ slice of the time-averaged data) are strongly curved at the beginning of the passage. According to the radial momentum equation,

$$\frac{\partial p}{\partial r} = \frac{\rho v^2}{r}, \quad (18)$$

the curvature of the inviscid flow in the cascade determines the radial pressure gradient (between the pressure and suction side). The pressure gradient results in a strong endwall crossflow from the pressure side to the suction side (Fig. 11).

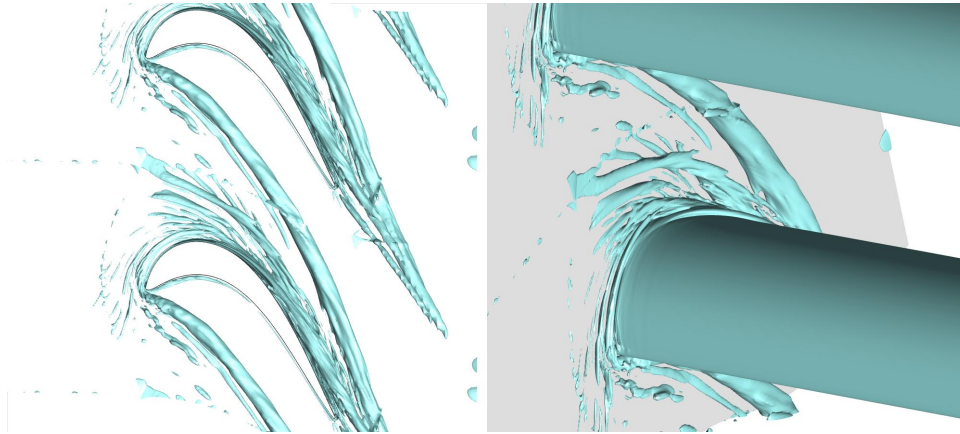


Figure 12. Time-average. Iso-surfaces of $Q = 10$.

Visualizations of the time-averaged flow-field (all time-averages were obtained for $6 < t < 12$) are provided in Fig. 12 - 14. The passage vortex, which is hard to make out in the instantaneous flow visualizations, clearly shows up in the time-averaged data. In addition to the passage vortex, a number of streamwise vortices of varying intensity are originating from the endwall (Fig. 12). The strong pitchwise endwall flow may lead to the downstream growth of steady crossflow vortices (in some instances the skin-friction lines are almost at a 90deg angle with respect to the streamlines; Fig. 11). The crossflow vortices may be “seeded” by numerical noise or by numerical inaccuracies associated with the singular grid point. To address the latter concern, the singular point could be moved farther upstream where the wall skin-friction lines follow the inviscid streamlines or a different grid topology could be conceived where the singular points are placed at entirely different locations.

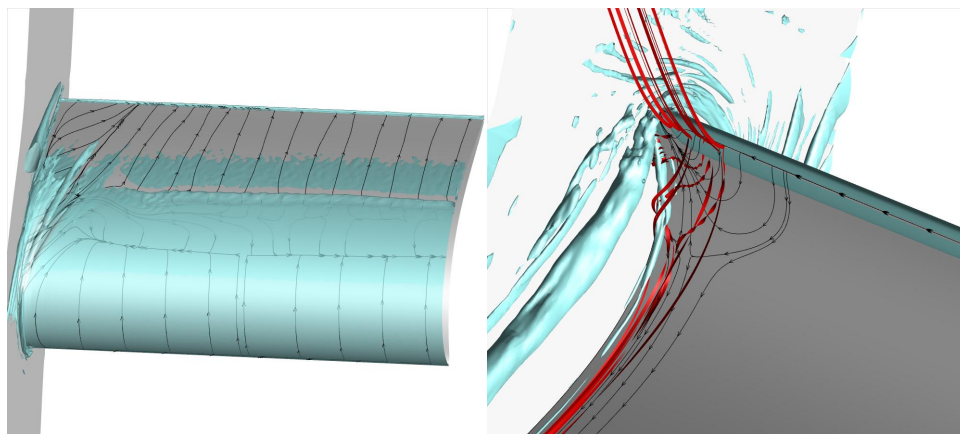


Figure 13. Iso-surfaces of $Q=60$ (left) and $Q=10$ (right) with skin-friction lines and streamlines.

The dominant structures on the suction side are a vortex associated with the 3-D trailing edge separation near the blade root (which results in a line of separation of the skin-friction lines) and a very narrow corner

vortex (Fig. 13). On the pressure side a short corner-vortex can be associated with a complicated 3-D flow separation near the leading edge. A comparison of the passage vortex location with the PIV measurements

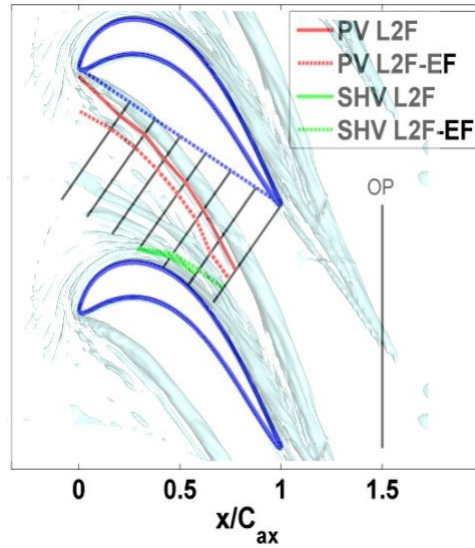


Figure 14. Location of Passage Vortex (PV) and Suction Side Horseshoe Vortex (SHV). Fig. 9a from Sangston et al.²⁵ overlaid with $Q=10$ iso-contours from present simulation.

by Sangston et al.²⁵ is provided in Fig. 14. Compared to the experiment the passage vortex is slightly closer to the suction side of the blade. The present simulations show no unique suction side vortex and, therefore, a comparison with the suction side horseshoe vortex in the experiment is not possible.

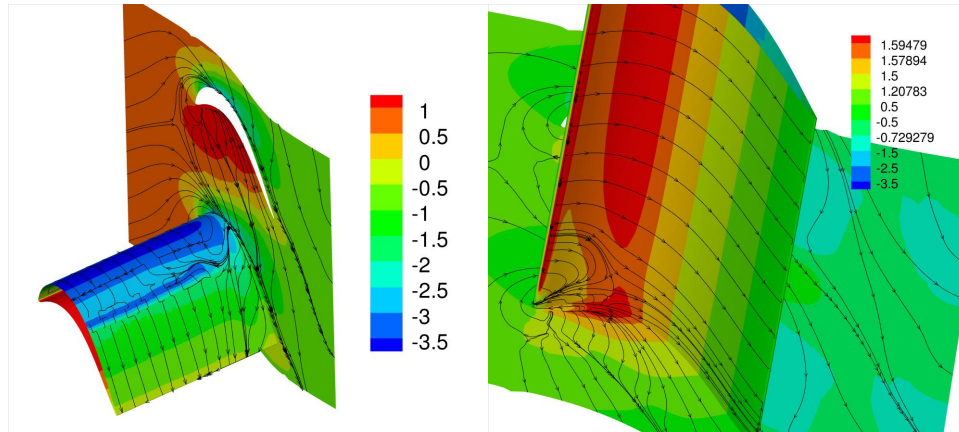


Figure 15. Wall pressure coefficient iso-contours and skin-friction lines.

Figure 15 provides wall-pressure iso-contours and skin-friction lines. The wall pressure increases rapidly at the end of the laminar separation bubble on the suction side of the blade. Near the leading edge, the corner vortices raise the pressure on the suction side and lower the pressure on the pressure side. In Fig. 16 iso-contours of the vorticity in the direction of the cascade outflow angle,

$$\omega_{out} = \omega_x \cos 60deg - \omega_y \sin 60deg , \quad (19)$$

are shown. The vorticity vector was computed as

$$\begin{bmatrix} \omega_x \\ \omega_y \\ \omega_z \end{bmatrix} = \begin{bmatrix} \partial/\partial x \\ \partial/\partial y \\ \partial/\partial z \end{bmatrix} \times \begin{bmatrix} u \\ v \\ w \end{bmatrix} . \quad (20)$$

The passage vortex is stronger and more coherent than the vortices on the suction side of the blade.

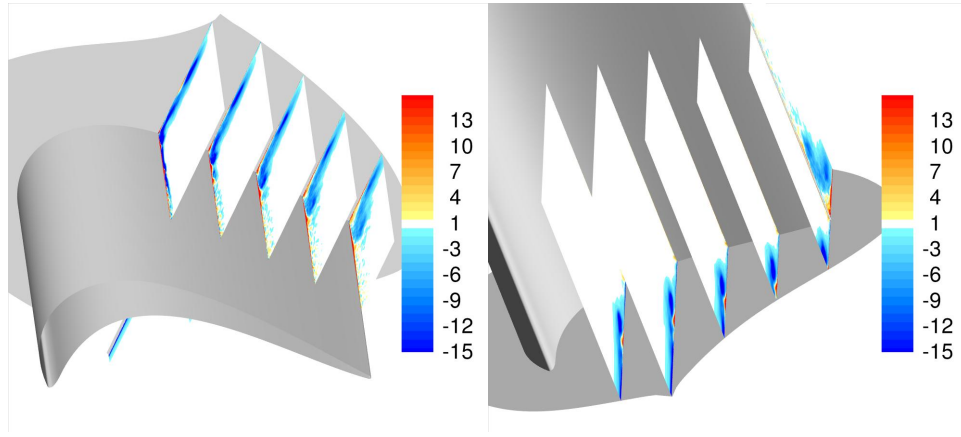


Figure 16. Iso-contours of vorticity magnitude, ω_{out} .

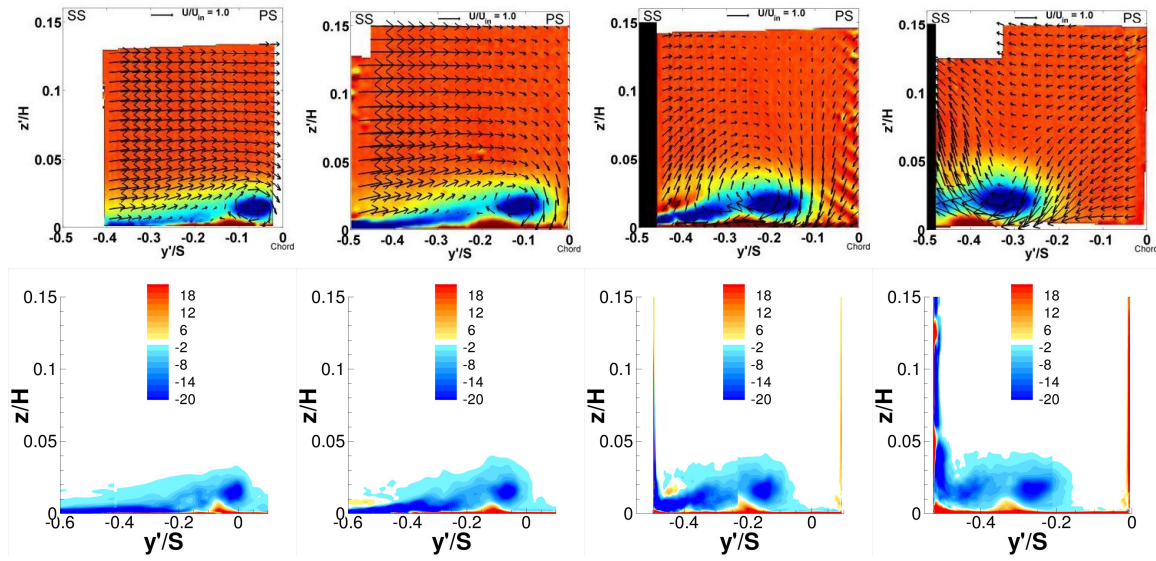


Figure 17. Vorticity iso-contours, $\omega_{x'}$, and in-plane velocity vectors. Top: PIV measurements by Sangston et al.²⁵ Bottom: Present results.

Iso-contours of the chord-wise vorticity, $\omega_{x'}$, for the four locations indicated in Fig. 9 are provided in Fig. 17. The agreement with the the PIV measurements by Sangston et al.²⁵ is adequate.

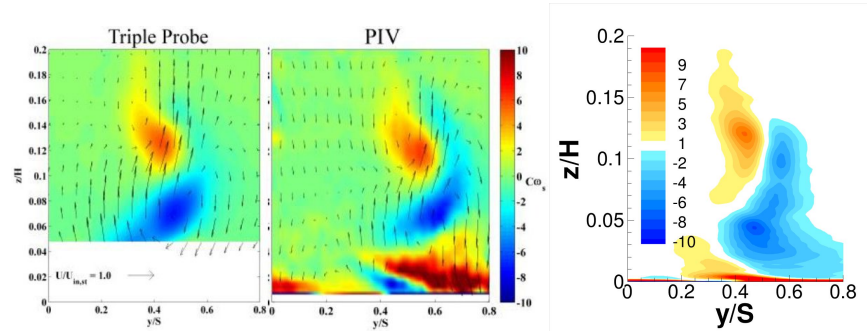


Figure 18. Iso-contours of ω_{out} at $x=1.5C_x$. PIV measurements by Sangston et al.²⁵ and present simulation.

Iso-contours of the streamwise vorticity, ω_{out} , at $x=1.5C_x$ in Fig. 18 show adequate agreement with the

triple probe data by Sangston et al.²⁵ The present near wall results are not in agreement with the PIV measurements by Sangston et al.²⁵ This may again be attributed to a lack of grid resolution (the grid resolution is degrading quickly downstream of the blade, see Fig. 2).

2. Blade With Fillet

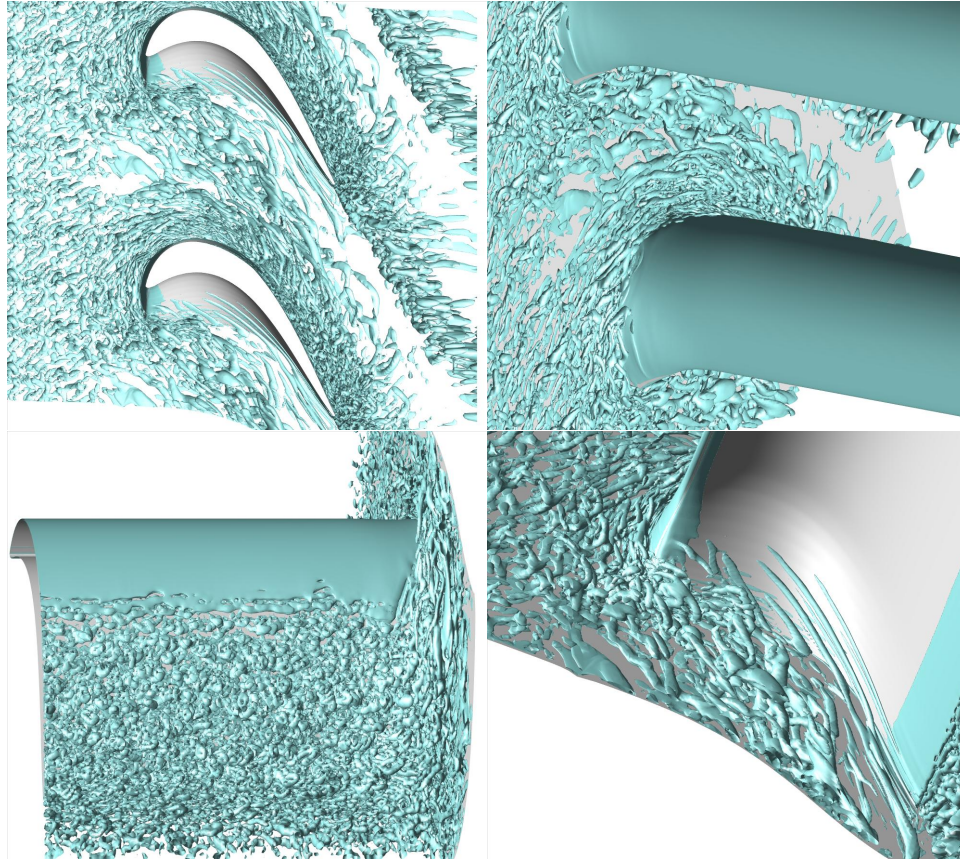


Figure 19. Instantaneous iso-surfaces of $Q = 10$.

Next the AFRL LPT geometry with endwall fillet (L2F-EF) was considered. Instantaneous flow visualizations are provided in Fig. 19. The endwall region near the pressure side of the blade is populated by elongated streamwise structures that are aligned parallel to each other (again indicating an instability). The skin-friction lines between the blades (Fig. 20) do not feature a line of separation and the $z = 0.05$ streamlines follow the suction side contour better than for the straight blade (Fig. 11).

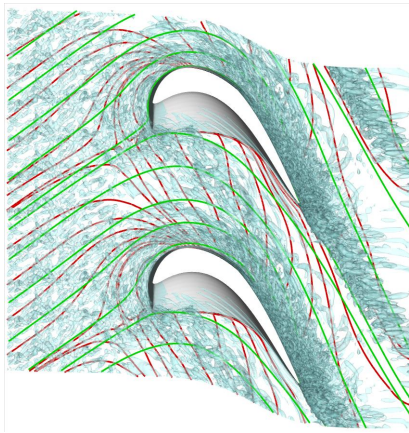


Figure 20. Instantaneous iso-surfaces of $Q = 10$. Red lines: Skin-friction lines for time average. Green lines: Streamlines at $z = 0.05$ for time-average.

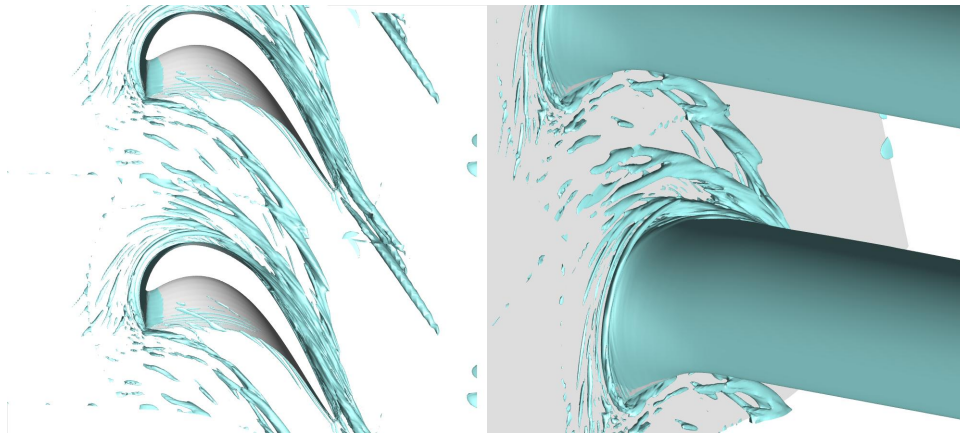


Figure 21. Time-average. Iso-surfaces of $Q = 10$.

Visualizations of the time-averaged flow field in Fig. 21 reveal that the passage vortex is significantly weaker than for the straight blade (Fig. 12). This is in agreement with the measurements.²⁵ The passage vortex trajectory does, however, not match up with the trajectory obtained from the PIV measurements²⁵ (Fig. 22). Skin-friction lines for the pressure surface of the fillet (Fig. 23) indicate attached flow while the skin-friction lines for the straight blade (Fig. 16) indicate separation and reverse flow. Iso-contours of the streamwise vorticity (Fig. 24) provide additional confirmation of a weakened passage vortex compared to the straight blade (Fig. 16).

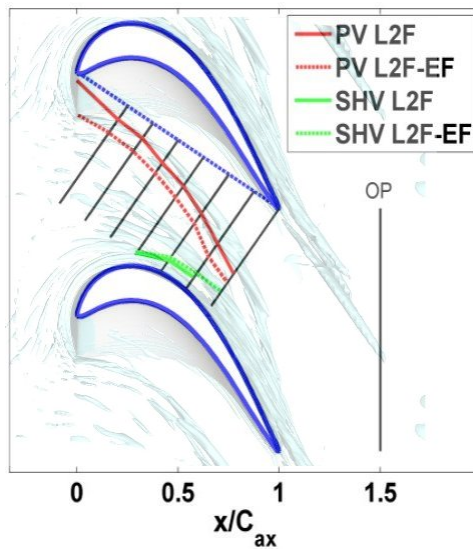


Figure 22. Location of Passage Vortex (PV) and Suction Side Horseshoe Vortex (SHV). Fig. 9a from Sangston et al.²⁵ overlaid with $Q=10$ iso-contours from present simulation.

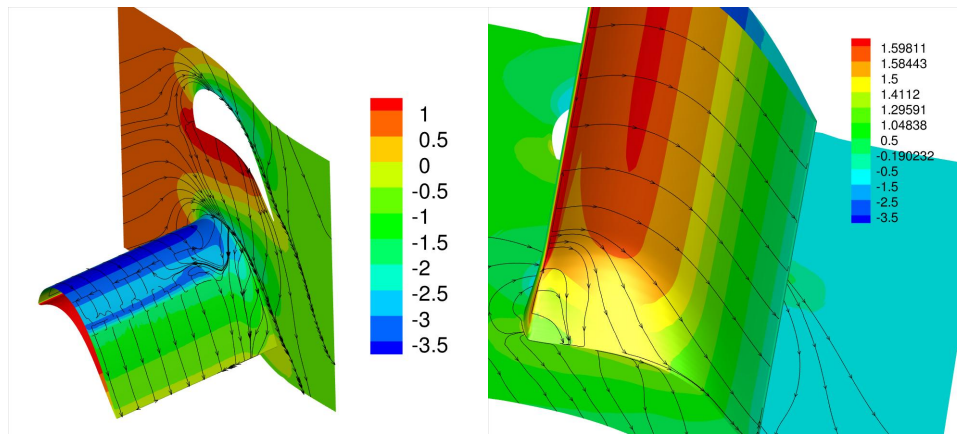


Figure 23. Wall pressure coefficient iso-contours and skin-friction lines.

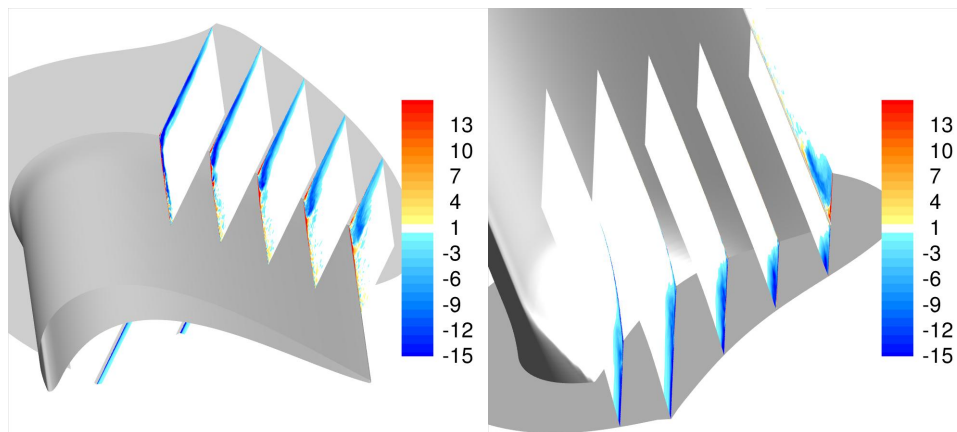


Figure 24. Iso-contours of vorticity magnitude, ω_{out} .

A comparison with PIV measurements by Sangston et al.²⁵ is provided in Fig. 25. The data are in qualitative agreement. In the experiment the suction side geometry of the L2F-EF was changed near the endwall: For ease of manufacturing, the fillet was machined as an extra piece that was added to the L2F geometry. As a result the recession on the suction side of the L2F-EF near the endwall was omitted in the experiment which may have a slight effect on the flow field. Vorticity iso-contours at the outflow boundary

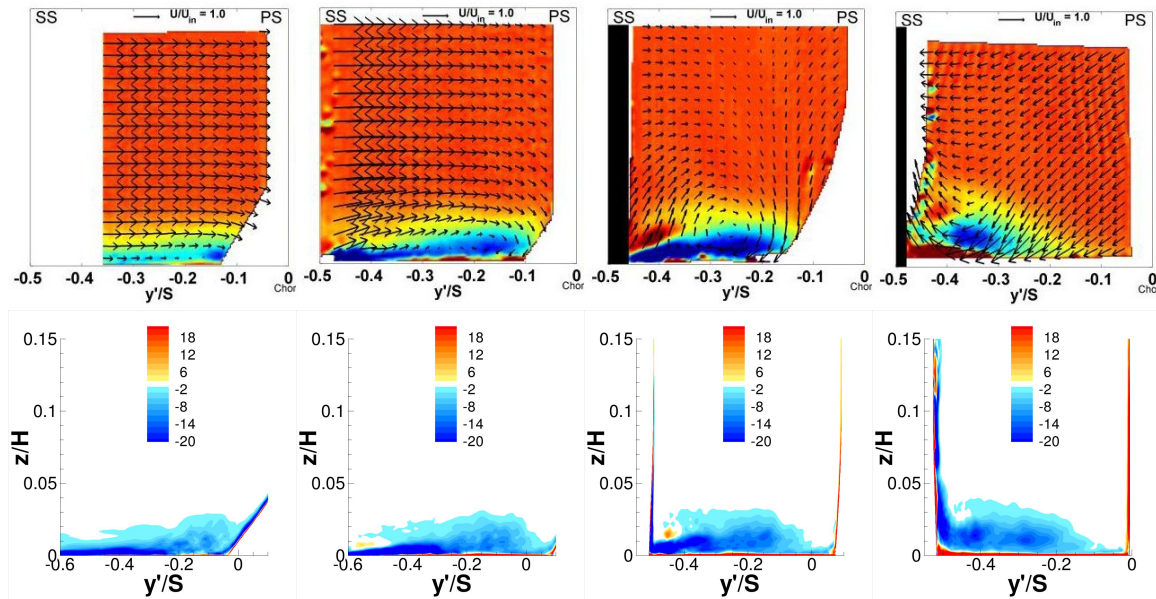


Figure 25. Vorticity iso-contours, $\omega_{x'}$, and in-plane velocity vectors. Top: PIV measurements by Sangston et al.²⁵ Bottom: Present results.

are shown in Fig. 26.

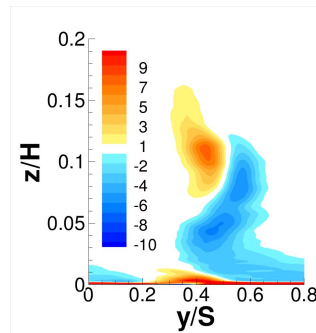


Figure 26. Iso-contours of ω_{out} at $x=1.5C_x$.

3. Comparison

Direct comparisons of the results for the L2F and L2F-EF geometry are provided in Figs. 27 & 28. The following observations can be made regarding the endwall (Fig. 27): With fillet the line of separation (as seen in the skin-friction lines for the straight blade) and the pressure dip (pressure iso-contours) associated with the passage vortex disappears and the streamlines at $z=0.05$ are better aligned in the outflow direction. Considering the blade suction surface, with fillet the spanwise width of the trailing edge separation at the endwall is reduced (Fig. 28).

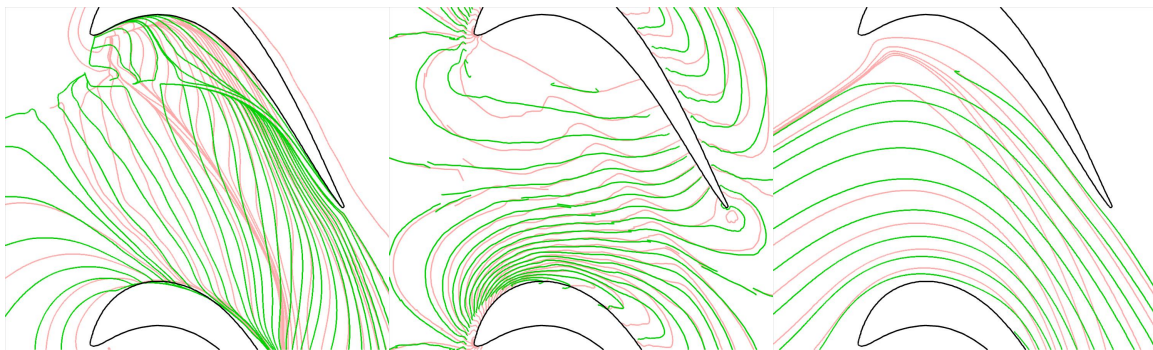


Figure 27. Skin-friction lines, wall-pressure iso-contours, and streamlines at $z=0.05$. Red lines: Straight blade. Green lines: Blade with fillet.

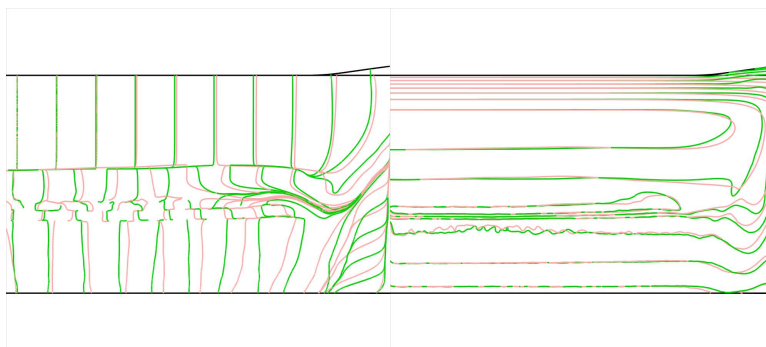


Figure 28. Suction side skin-friction lines and wall-pressure iso-contours. Red lines: Straight blade. Green lines: Blade with fillet.

B. Laminar Endwall Boundary Layer

1. Straight Blade (No Fillet)

When the approach flow endwall boundary layer is laminar, traveling wave structures appear upstream of the cascade inflow hinting at the existence of an instability mechanism (Fig. 29). As for the turbulent endwall boundary layer (Fig. 10) the endwall region near the pressure side of the blade is relatively “quiet”. Neither the skin-friction lines nor the streamlines hint at the existence of a pronounced passage vortex (Fig. 30). This conclusion is supported by visualizations of the time-averaged flow (Fig. 31). A wall-tangential streamwise vortex that is about one third of the blade spacing displaced from the suction side of the blade is seen in the time-average. A similar structure can also be observed for the turbulent endwall boundary layer albeit with much reduced coherence (Fig. 12). For the laminar endwall boundary layer the vortex originates from a region where the skin-friction lines form a saddle point (Figs. 30 & 31).

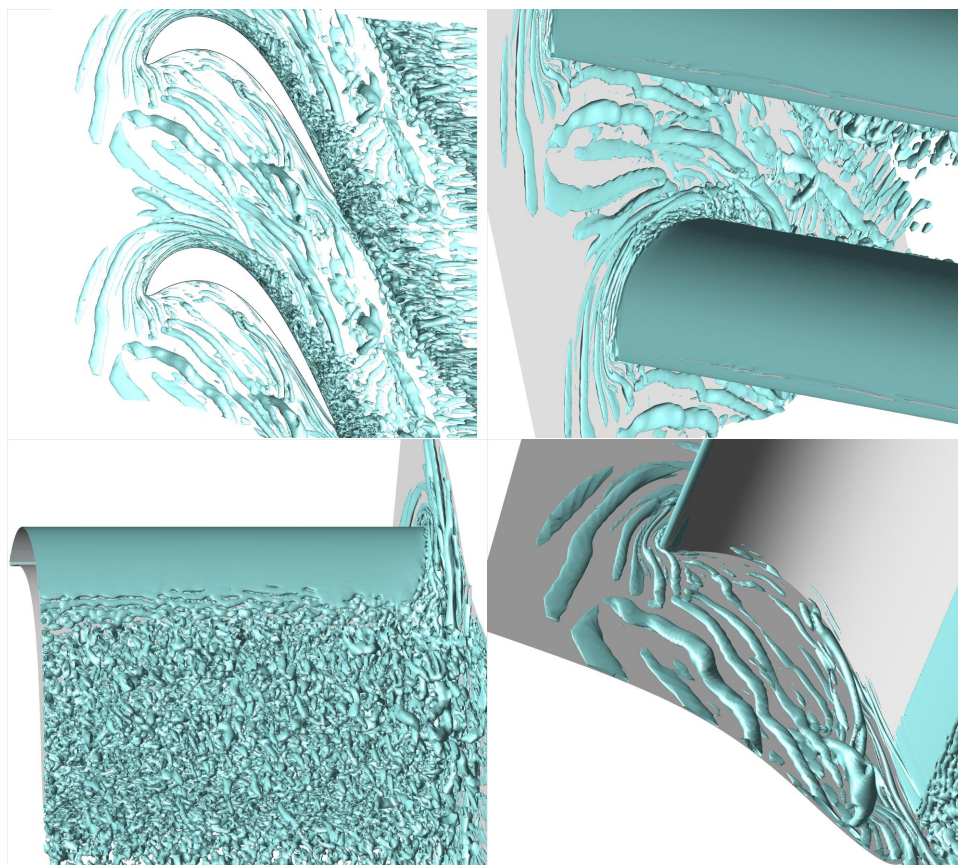


Figure 29. Iso-surfaces of $Q = 10$.

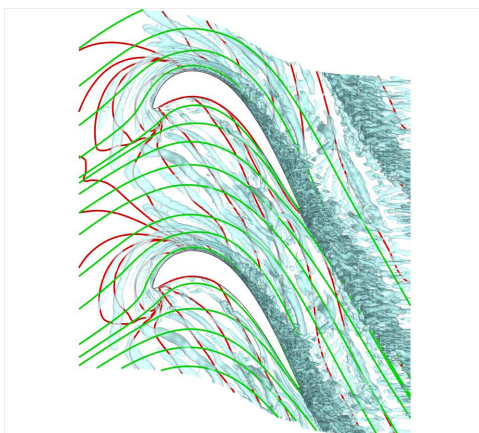


Figure 30. Instantaneous iso-surfaces of $Q = 10$. Red lines: Wall skin-friction lines for time average. Green lines: Streamlines at $z = 0.05$ for time-average.

A comparison of Figs. 15 (turbulent endwall boundary layer) and 32 (laminar endwall boundary layer) reveals that for the latter the suction side trailing edge separation is reduced and the pressure side separation is almost absent.

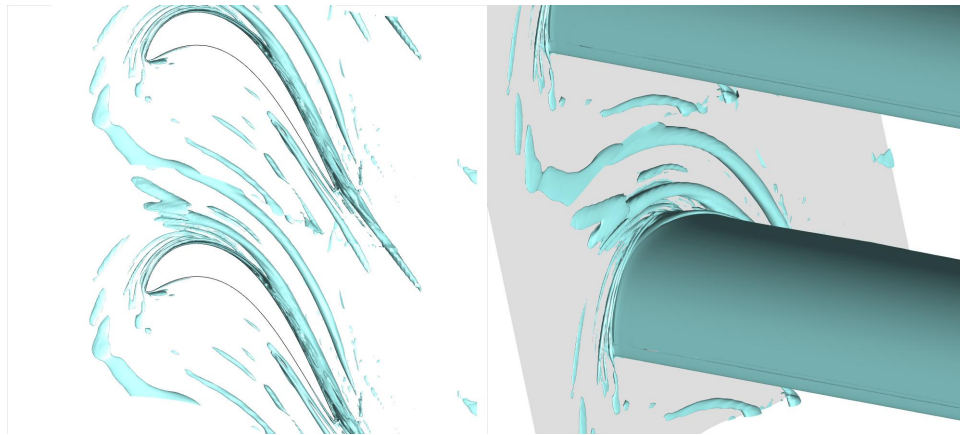


Figure 31. Time-average. Iso-surfaces of $Q = 10$.

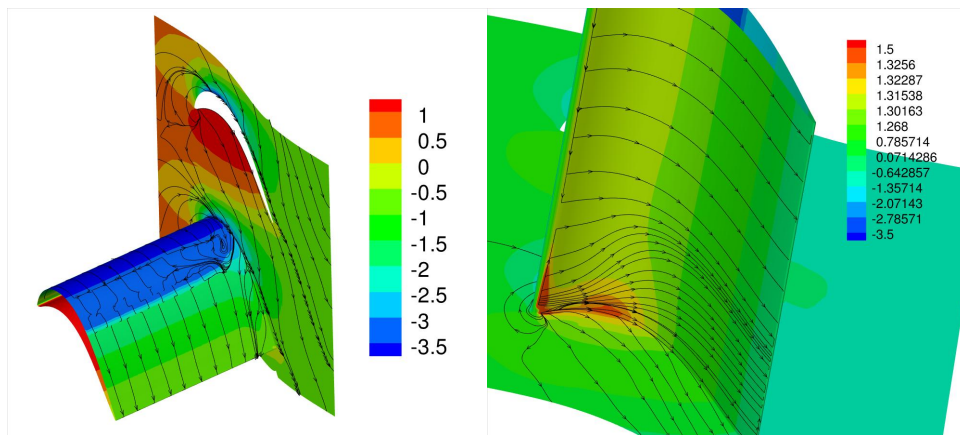


Figure 32. Wall pressure coefficient iso-contours and skin-friction lines.

Finally, a comparison of Figs. 16 & 33 and Figs. 17 & 34 provides support for the statement that the passage vortex is virtually missing for the laminar endwall boundary layer.

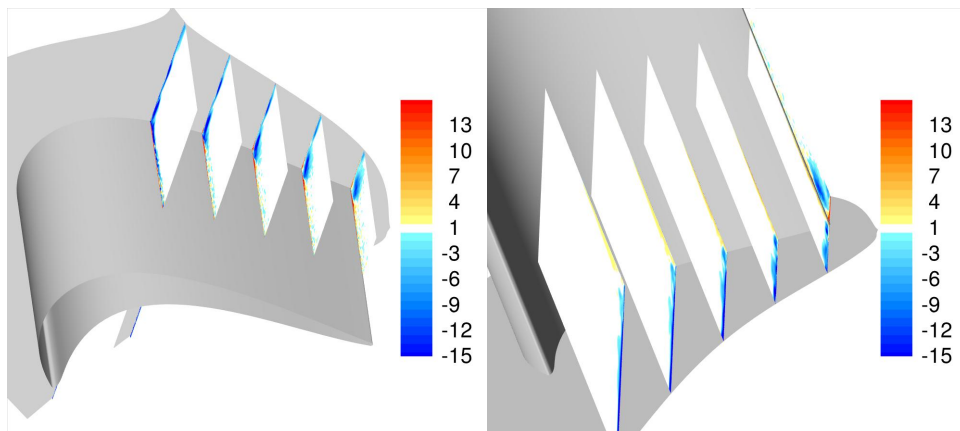


Figure 33. Time-average. Iso-contours of vorticity magnitude, ω_{out} .

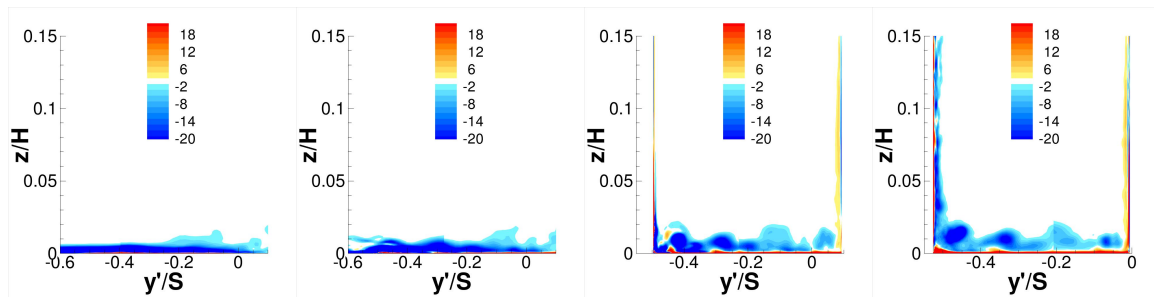


Figure 34. Vorticity iso-contours, $\omega_{x'}$.

For completeness, vorticity contours for the outflow plane are shown in Fig. 35.

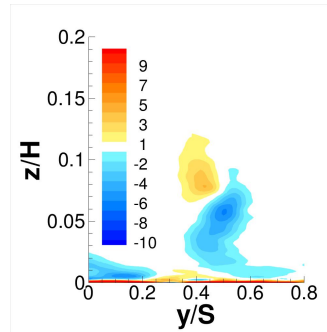


Figure 35. Iso-contours of ω_{out} at $x=1.5C_x$.

2. Blade With Fillet

Finally, the L2F-EF geometry with laminar endwall boundary layer was investigated. For this simulation the fifth-order-accurate discretization for the convective terms was chosen. Instantaneous iso-surfaces of the Q vortex identification criterion in Fig. 36 & 37 reveal a hairpin structure upstream of the blade and several similar structures downstream of the leading edge. Also, similar to the simulation for the turbulent endwall boundary layer (Fig. 19), streamwise structures can be observed on the pressure side near the endwall.

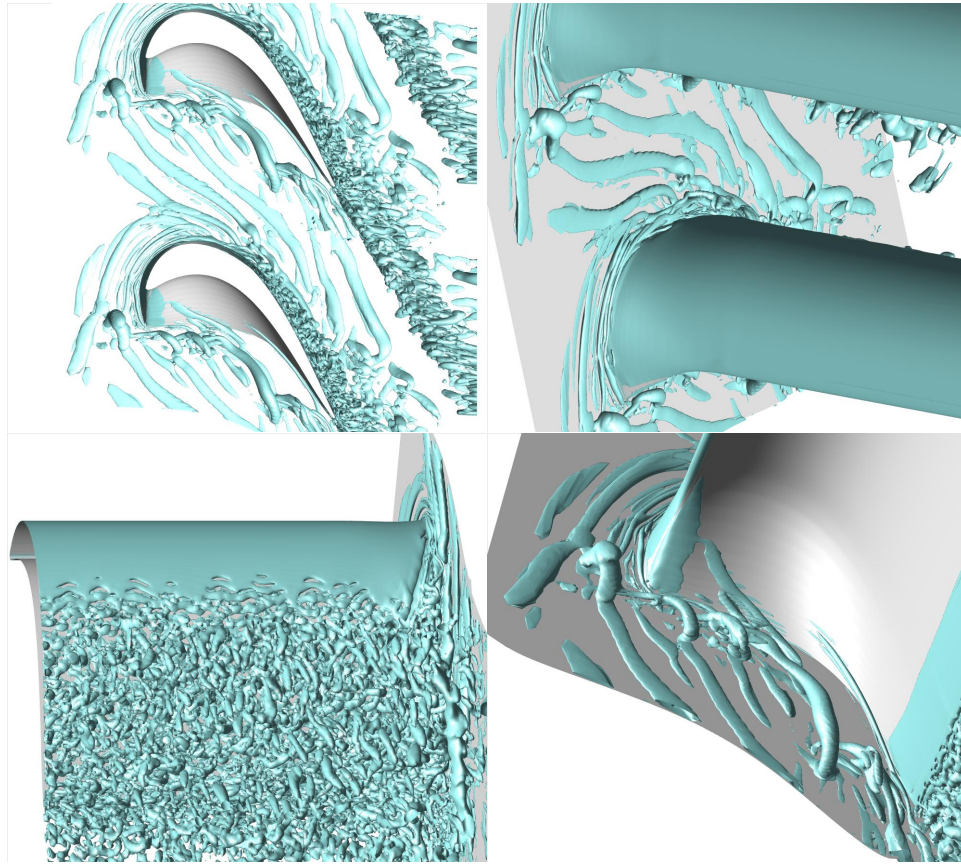


Figure 36. Iso-surfaces of $Q = 10$.

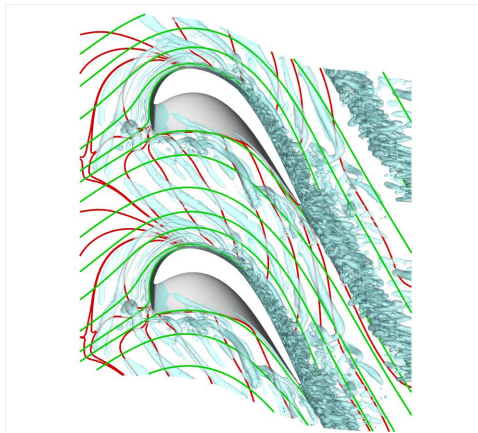


Figure 37. Instantaneous iso-surfaces of $Q = 10$. Red lines: Wall skin-friction lines for time average. Green lines: Streamlines at $z = 0.05$ for time-average.

With fillet a passage vortex is originating at the leading edge of the blade (Fig. 38). The vortex remains close to the pressure side of the blade and dissipates shortly downstream of the trailing edge. Interestingly, for the straight blade with laminar endwall (Fig. 31) the passage vortex is missing. This is contrast to the results for the turbulent endwall boundary layer. One must conclude that the endwall boundary layer state has a large impact on the mean flow field. However, caution is in order as the two simulations were not carried out with the same discretization.

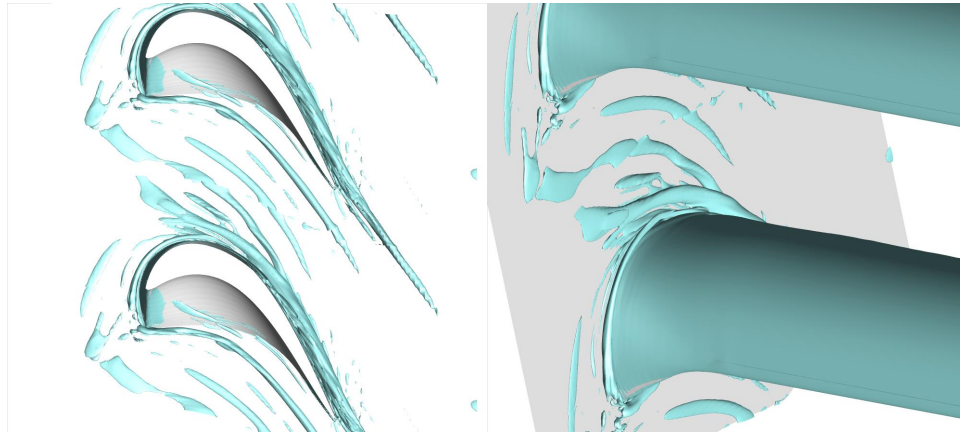


Figure 38. Time-average. Iso-surfaces of $Q = 10$.

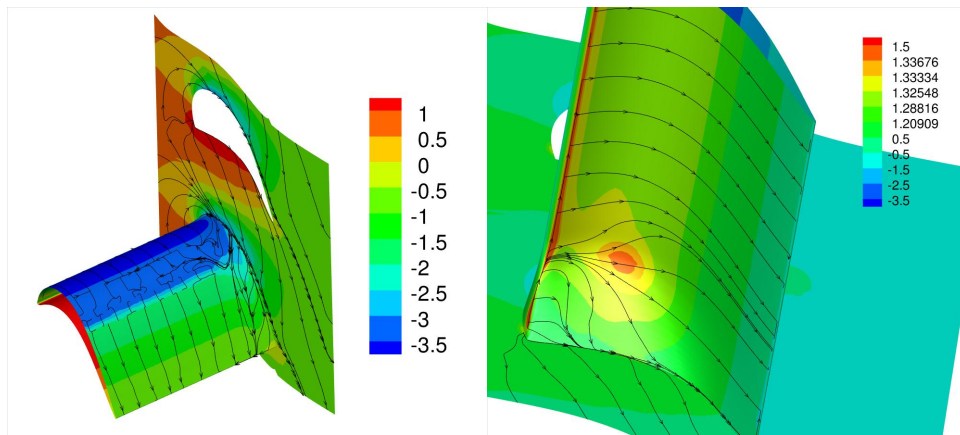


Figure 39. Wall pressure coefficient iso-contours and skin-friction lines.

The skin-friction lines and pressure iso-contours in Fig. 39 are qualitatively similar to the results for the turbulent endwall boundary layer (Fig. 23). The suction side trailing edge corner separation is narrower for the laminar endwall boundary layer.

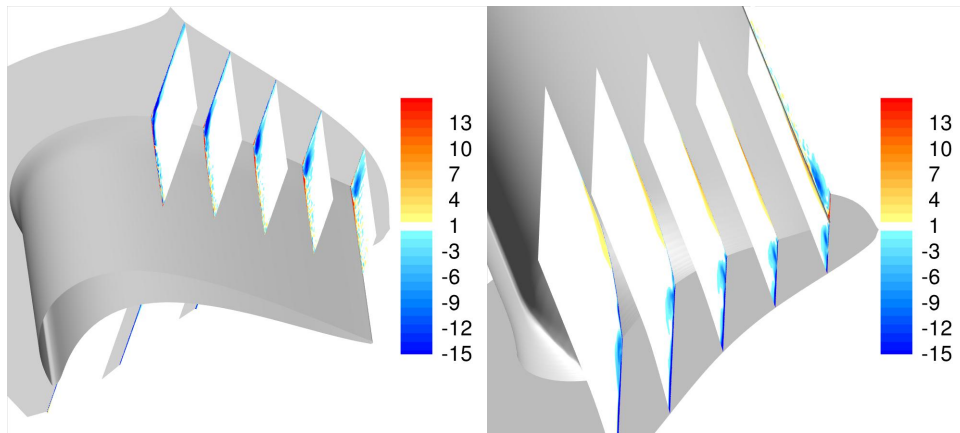


Figure 40. Time-average. Iso-contours of vorticity magnitude, ω_{out} .

Iso-contours of the vorticity in the cascade (Fig. 40) provide proof of a strong suction side corner vortex.

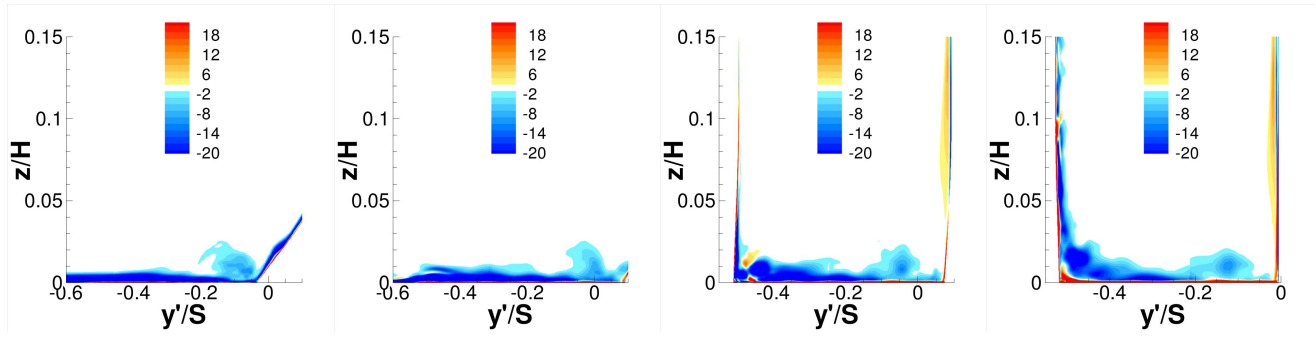


Figure 41. Laminar endwall boundary layer (grid 4). Vorticity iso-contours, $\omega_{x'}$.

The passage vortex is visible in Fig. 41. It remains close to the pressure side. Iso-contours of the

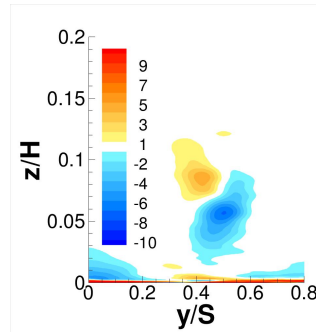


Figure 42. Iso-contours of ω_{out} at $x=1.5C_x$.

streamwise vorticity, ω_{out} , at the outflow plane are shown in Fig. 42.

3. Comparison

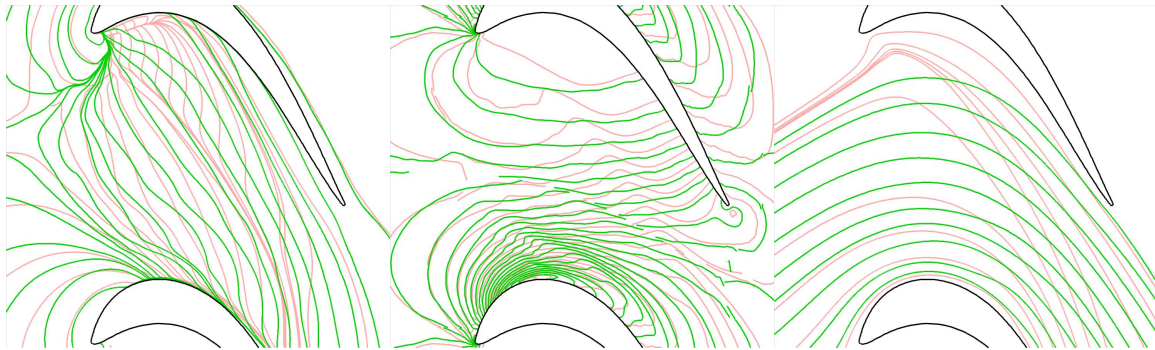


Figure 43. Skin-friction lines, wall-pressure iso-contours, and streamlines at $z=0.05$. Red lines: Turbulent endwall boundary layer. Green lines: Laminar endwall boundary layer.

Direct comparisons of the results for the straight blade with turbulent and laminar endwall boundary layer are provided in Figs. 43 & 44. The boundary layer state has a strong effect on the endwall flow. The most prominent differences are the lack of the passage vortex, a reduced suction side trailing edge corner separation, and a more two-dimensional pressure distribution on the suction side for the laminar endwall boundary layer.

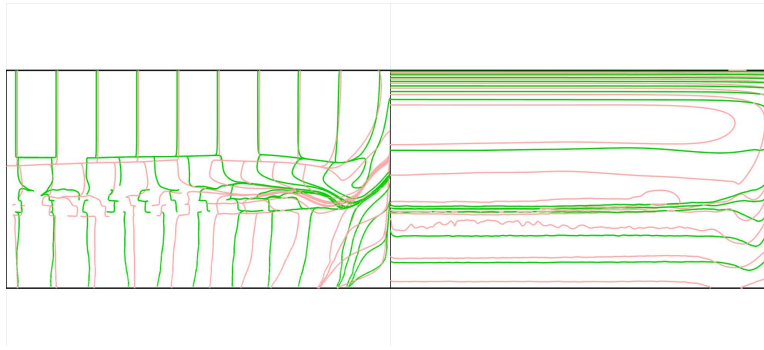


Figure 44. Suction side skin-friction lines and wall-pressure iso-contours. Red lines: Turbulent endwall boundary layer. Green lines: Laminar endwall boundary layer.

C. Total Pressure Loss Coefficient

Table 4 lists the mass-averaged total pressure, dynamic pressure, and total pressure loss coefficient for the different cases as well as for the RANS calculations by Lyall et al.²⁴ and the experiments by Sangston et al.²⁵ The total pressure loss coefficient for the turbulent endwall boundary layer is 29% (straight blade) and 25% (blade with fillet) higher than for the laminar endwall boundary layer. This once again illustrates the strong dependence of the flow on the endwall boundary layer state. For the turbulent endwall boundary layer the fillet reduces the loss coefficient by 8.0% (9.9% reduction in experiment). In general, the loss coefficient for the RANS calculations by Lyall et al.²⁴ and the experiments by Sangston et al.²⁵ is higher than for the present simulations. This may be explained by differences in the postprocessing of the data (i.e., the computation of the total pressure loss coefficient), by a lack of grid resolution, or by differences w.r.t. the endwall boundary layer state.

Case	$c''_{p,0,in}$	q''_{in}	$c''_{p,0,out}$	q''_{out}	Y_{tot}
Straight blade					
Turbulent endwall B.L.	0.65876	0.47128	0.54411	1.1148	0.1147
Laminar endwall B.L.	0.47889	0.46077	0.38966	1.0883	0.08923
RANS, Lyall et al. ²⁴					0.141
Experiment, Sangston et al. ²⁵					0.142
Blade with fillet					
Turbulent endwall B.L.	0.65720	0.47159	0.55169	1.1166	0.1055
Laminar endwall B.L.	0.48802	0.46246	0.40381	1.0908	0.08421
RANS, Lyall et al. ²⁴					0.131
Experiment, Sangston et al. ²⁵					0.128

Table 4. Mass-averaged total pressure coefficient, $c''_{p,0}$, and dynamic pressure, q'' . Total pressure loss coefficient, Y_{tot} .

IV. Conclusions

Three-dimensional Implicit Large Eddy Simulations (ILES) of the L2F blade with and without fillet were carried out for a Reynolds number based on axial chord of $Re=100,000$. Both a laminar and a turbulent endwall boundary layer were considered. The results for the straight blade (no fillet) with turbulent endwall boundary layer are in adequate agreement with Particle Image Velocimetry (PIV) measurements by Sangston et al.²⁵ A strong passage vortex and a considerable suction side trailing edge separation are observed. Both are total pressure loss mechanisms and amenable to flow control. The simulation for the L2F blade with fillet (L2F-EF geometry) and turbulent endwall boundary layer indicates a greatly reduced coherence of the passage vortex in accordance with the experimental findings. Overall, the total pressure loss coefficient for

both simulations is lower than in the experiment. This may be attributed to insufficient grid resolution. As a result the endwall boundary layer is too thin. Simulations with laminar endwall boundary layer (i.e., the thinnest possible boundary layer) revealed that the endwall boundary layer has a profound effect of the flow topology. For the straight blade (no fillet) and with laminar endwall boundary layer the passage vortex is missing and the total pressure loss coefficient is greatly reduced (compared to the case with turbulent endwall boundary layer). With fillet a weak passage vortex is obtained. The results for the turbulent and laminar endwall boundary layer are diametrically opposed: For the turbulent endwall boundary layer the fillet suppresses the passage vortex. For the laminar endwall boundary layer the fillet generates the passage vortex. This strong dependence of the flow topology on the endwall boundary layer state is one of the most interesting outcomes of the present investigation.

Overall, the mean flow topology and the mechanisms resulting in the observed unsteady coherent structures remain poorly understood. One of the objectives of the project was to employ unsteady Active Flow Control (AFC) near the endwall to probe instabilities. Due to the unexpected complexity of the endwall flow simulations and the simulation turnaround times (a typical simulation required four days on 256 processors) the planned AFC simulations could not be accomplished. The following tasks are planned for the future: The dependence of the results on the grid resolution and the accuracy of the numerical discretization will be investigated. The computational domain for generating the turbulent endwall boundary layer was quite narrow and resulted in a pitchwise periodicity of the endwall boundary layer. The narrow approach flow domain will be replaced by a wider domain. Simulations at a reduced Reynolds number (e.g., $Re=25,000$) are less costly and, should the physics be similar, will be considered for investigating the endwall flow physics. Hybrid turbulence models are a tempting alternative but the transitional nature of the flow raises questions with respect to the applicability of the approach. The time-dependent flow data will be analyzed in more detail with the Proper Orthogonal Decomposition (POD),^{33,34} and based on the analysis different Active Flow Control (AFC) strategies will be proposed.

Acknowledgments

This research was carried out during a summer research fellowship of the first author at the U.S. Air Force Research Laboratory at Wright-Patterson Air Force Base. The fellowship was made possible and sponsored through the Air Force Summer Faculty Fellowship Program. High Performance Computing (HPC) resources were provided by the Department of Defense HPC Modernization Program.

References

- ¹Dunn, M.G., "Convective Heat Transfer and Aerodynamics in Axial Flow Turbines," *J. Turbomachinery*, Vol. 123, 2001, pp. 637-686
- ²Howell, R.J., Hodson, H.P., Schulte, V., Stieger, R.D., Schiffer, H., Haselbach, F., and Harvery, N.W., "Boundary Layer Development in the BR710 and BR715 LP Turbines - The Implementation of High-Lift and Ultra-High-Lift Concepts," *J. Turbomachinery*, Vol. 124, 2002, pp. 385-392
- ³Korakianitis, T., "Prescribed-Curvature-Distribution Airfoils for the Preliminary Geometric Design of Axial-Turbomachinery Cascades," *J. Turbomachinery*, Vol. 115, 1993, pp. 325-333
- ⁴Korakianitis, T., and Papagiannidis, P., "Surface-Curvature-Distribution Effects on Turbine-Cascade Performance," *J. Turbomachinery*, Vol. 115, 1993, pp. 334-340
- ⁵Sieverding, C.H., "Recent Progress in the Understanding of Basic Aspects of Secondary Flows in Turbine Blade Passages," *J. Eng. Gas Turbines Power*, Vol. 107, 1985, pp. 248-257
- ⁶Wang, H.P. Olson, S.J., Goldstein, R.J., and Eckert, E.R.G., "Flow Visualization in a Linear Turbine Cascade of High Performance Turbine Blades," *J. Turbomachinery*, Vol. 109, 1997, pp. 1-8
- ⁷Langston, L., "Secondary flows in axial turbines - A review," *Annals of the New York Academy of Sciences: Heat Transfer in Gas Turbine Systems*, Vol. 934, 2001, pp. 11-26
- ⁸Weiss, A.P. and Fottner, L., "The Influence of Load Distribution on Secondary Flow in Straight Turbine Cascades," *J. Turbomachinery*, Vol. 117, 1995, pp. 133-141
- ⁹Zoric, T., Popovic, I., Sjolander, S.A., Praisner, T., and Grover, E., "Comparative Investigation of Three Highly Loaded LP Turbine Airfoils: Part I - Measured Profile and Secondary Losses at Design Incidence," ASME Paper GT2007-27537, 2007
- ¹⁰Knezevici, D.C., Sjolander, S.A., Praisner, T.J., Allen-Bradley, E., and Grover, E.A., "Measurements of Secondary Losses in a High-Lift Front-Loaded Turbine Cascade with the Implementation of Non-Axisymmetric Endwall Contouring," ASME Paper GT2009-59677, 2009
- ¹¹Praisner, T.J., Grover, E.A., Knezevici, D.C., Popovic, I., Sjolander, S.A., Clark, J.P., and Sondergaard, R., "Toward the Expansion of Low-Pressure Turbine Airfoil Design Space," ASME Paper GT2008-50898, 2008

- ¹²Lyall, M.E., "Effects of Front-Loading and Stagger Angle on Endwall Losses of High Lift Low Pressure Turbine Vanes," Ph.D. Dissertation, Air Force Institute of Technology, 2012
- ¹³Sauer, H., Muller, R., and Vogeler, K., "Reduction of Secondary Flow Losses in Turbine Cascades by Leading Edge Modifications at the Endwall," *J. Turbomachinery*, Vol. 123, No. 2, 2001, pp. 207-213
- ¹⁴Zess, G., and Thole, K., "Computational Design and Experimental Evaluation of Using a Leading Edge Fillet on a Gas Turbine Vane," *J. Turbomachinery*, Vol. 124, No. 2, 2002, pp. 167-175
- ¹⁵Becz, S., Majewski, M., and Langston, L., "An experimental investigation of contoured leading edges for secondary flow loss reduction," ASME Paper GT2004-53964, 2004
- ¹⁶Saha, A.K., Mahmood, G.I., and Acharya, S., "The Role of Leading-Edge Contouring on End-wall Flow and Heat Transfer: Computations and Experiments," ASME Paper GT2006-91318, 2006
- ¹⁷Harrison, S., "The Influence of Blade Lean on Turbine Losses," *J. Turbomachinery*, Vol. 114, 1992, pp. 184-190
- ¹⁸Rose, M.G., "Non-Axisymmetric Endwall Profiling in the HP NGV's of an Axial Flow Gas Turbine," ASME Paper 94-GT-249, 1994
- ¹⁹Harvey, N., Rose, M., Taylor, M., Shahpar, S., Hartland, J., and Gregory-Smith, D., "Nonaxisymmetric turbine end wall design: Part I - Three-dimensional linear design system," *J. Turbomachinery*, Vol. 11, No. 2, 2000, pp. 278-285
- ²⁰Hartland, J., Gregory-Smith, D., Harvey, N., and Rose, M., "Nonaxisymmetric turbine end wall design: Part II Experimental validation," *J. Turbomachinery*, Vol. 122, No. 2, 2000, pp. 286-293
- ²¹Praisner, T., Allen-Bradley, E., Grover, E., Knezevici, D., and Sjolander, S., "Application of non-axisymmetric endwall contouring to conventional and high-lift turbine airfoils," *J. Turbomachinery*, Vol. 135, No. 6, 2013, pp. 061006-1-8
- ²²Bagshaw, D.A., Gregory-Smith, D.G., Ingram, G.L., and Stokes, M.R., "A Turbine Cascade Facility for Secondary Flow Research," ASME Paper GT2006-90868, 2006
- ²³McIntosh, J., MacPherson, R., Ingram, G., and Hogg, S., "Profiled Endwall Design using Genetic Algorithms with Different Objective Functions," ASME Paper GT2011-45836, 2011
- ²⁴Lyall, M.E., King, P.I., Clark, J.P., Sondergaard, R., "Endwall Loss Reduction of High Lift Low Pressure Turbine Airfoils Using Profile Contouring - Part I: Airfoil Design," ASME Paper GT2013-95000, 2013
- ²⁵Sangston, K., Little, J., Lyall, M.E., and Sondergaard, R., "Endwall Loss Reduction of High Lift Low Pressure Turbine Airfoils Using Profile Contouring - Part II: Validation," ASME Paper GT2013-95002, 2013
- ²⁶McQuilling, M.W., "Design and Validation of a High Lift Low-Pressure Turbine Blade," Ph.D. Dissertation, Wright State University, Dayton, OH, 2007
- ²⁷Gross, A., and Fasel, H. F., "High-Order-Accurate Numerical Method for Complex Flows," *AIAA Journal*, Vol. 46, No. 1, 2008, pp. 204-214
- ²⁸Gross, A., and Fasel, H.F., 2008, "Multi-block Poisson grid generator for cascade simulations," *Mathematics and Computers in Simulation*, Vol. 79, No. 3, 2008, pp. 416-428
- ²⁹Georgiadis, N.J., Rizzetta, D.P., and Fureby, C., "Large-Eddy Simulation: Current Capabilities, Recommended Practices, and Future Research," *AIAA Journal*, Vol. 48, No. 8, 2010, pp. 1772-1784
- ³⁰Gross, A., and Fasel, H.F., "Characteristic Ghost-Cell Boundary Condition," *AIAA Journal*, Vol. 45, No. 1, 2007, pp. 302-306
- ³¹Baines, P.G., Majumdar, S.J., and Mitsudera, H., "The mechanics of the Tollmien-Schlichting wave," *J. Fluid Mech.*, Vol. 312, 1996, pp. 107-124
- ³²Hunt, J.C.R., Wray, A.A., and Moin, P., "Eddies, stream, and convergence zones in turbulent Flows," Report CTR-S88, Center For Turbulence Research, Stanford, CA, 1988
- ³³Lumley, J.L., "The Structure of Inhomogeneous Turbulent Flows," *Atmospheric turbulence and radio wave propagation*, Nauka, Moscow and Toulouse, France, eds. Yaglom and Tatarsky, 1967, pp. 166-178
- ³⁴Sirovich, L., "Turbulence and the dynamics of coherent structures, Part I-III," *Quarterly of Applied Mathematics*, Vol. 45, 1987, pp. 561-590